https://doi.org/10.5194/egusphere-2026-4143
Preprint. Discussion started: 17 August 2026

Supraglacial lake bathymetry from high-resolution airborne imagery using stereophotogrammetry and structure from motion

Michael Studinger[1], C. Wayne Wright[2,3], Oleg Alexandrov[4,5]

[1]Cryospheric Sciences Laboratory, NASA Goddard Space Flight Center, Greenbelt, MD 20771, USA
[2]C. W. Wright Consulting, Tampa, FL 33544, USA
[3]Science Systems and Applications, Inc., Lanham, MD 20706, USA
[4]Intelligent Robotics Group, NASA Ames Research Center, Moffett Field, CA 94035, USA
[5]KBR Wyle Services, Moffett Field, CA 94035, USA

Correspondence to: Michael Studinger (michael.studinger@nasa.gov)

Abstract. Understanding the hydrological system of the ice sheet of Kalaallit Nunat (Greenland, GrIS) requires observational knowledge on a range of scales with varying spatial and temporal resolutions and coverage. In general, process-related studies require high-resolution observations over regional scales spanning hundreds of kilometers. The spatial resolution of spaceborne imaging is continually improving, however, airborne imaging can provide complementary information at higher resolution and can combing multiple sensors with coincident data acquisition. Here we use regional-scale, high-resolution (10×10 cm) aerial imagery collected by NASA's Airborne Topographic Mapper instrument suite (ATM) to derive bathymetry of supraglacial lakes and streams using Structure from Motion (SfM) and stereo processing techniques. SfM uses multiple overlapping images and iterative bundle adjustment to solve and optimize camera positions and parameters. Stereophotogrammetry requires highly accurate camera geometry and calibration. Supraglacial lakes appear as distinct blue features in natural-color imagery of the ice sheet with often clearly visible features at the lake bottom, making them ideal for SfM and stereo processing. The ATM airborne data also includes two coincident green (532 nm) small footprint lidar providing a rare opportunity to compare lidar and imagery-based bathymetry methods.

We use the NASA Ames Stereo Pipeline (ASP), a powerful open-source processing toolbox with a long legacy, a broad user community, and active tool development. We compare the ASP stereo bathymetry with lake depth estimates from a commercial SfM package and bathymetric estimates from our coincident lidar data. Our results show that supraglacial lake bathymetry can be mapped at high spatial resolution using stereophotogrammetry and SfM reconstruction of topobathymetric digital elevation models (DEMs). The stereographic method we use accurately accounts for refraction in water. The SfM approach uses an iterative refraction correction for SfM to accurately determine the lake bottom topography. We find two main limitations for image-based bathymetry estimates: thin lake ice cover can obscure lake bottom features making feature tracking between images impossible. The second limitation comes from caustics at the lake bottom caused by refraction of sunlight on moving surface waves. These caustics are not stationary patterns and can move in the 0.5 secs between image acquisitions ruling out static feature tracking necessary for SfM or stereophotogrammetry. Each method has its own limitations and biases. By analyzing changes in the shape of lidar waveforms between survey targets with no differential penetration and supraglacial

https://doi.org/10.5194/egusphere-2026-4143
Preprint. Discussion started: 17 August 2026

lakes we have shown for the first time that green photons can penetrate below the lake bottom surface resulting in a range and therefore elevation bias.

1 Introduction

The Greenland Ice Sheet (GrIS) experiences surface melting between late spring and early fall primarily around its perimeter where surface elevations are typically lower than in the interior (e.g., Howat et al., 2014) and surface temperatures are more likely to reach melting conditions than in the interior (e.g., Hall et al., 2018). The seasonal meltwater transforms the frozen surface of the ice sheet into a wet environment, with meltwater pooling in supraglacial lakes connected by a dendritic pattern of meandering streams and rivers (e.g., Chu, 2014; Nienow et al., 2017; Pitcher and Smith, 2019; Studinger et al., 2022a). Runoff from meltwater now exceeds mass loss from ice discharge and basal melting (Enderlin et al., 2014; Van Den Broeke et al., 2016) and dominates mass loss of the GrIS (Otosaka et al., 2023; The IMBIE Team, 2020). Therefore, the formation of meltwater affects ice sheet mass balance and stability.

The lakes appear as distinct blue features in natural color (red, green, and blue; RGB) images with deep parts of the lakes typically showing darker blue colors compared to shallow parts (Figure 1). The lakes grow throughout the melt season and typically reach several hundreds of meters in size and over 10 meters in depth. The water in the lakes is very clear with low turbidity resulting in good visibility of features on the lake bottom such as crevasses and lake bottom texture in areas with open water. The lakes can be covered by thin translucent ice in particular at the beginning and end of the melt season (Figure 1). Translucent ice cover often appears as milky, cloudy, or frosted layers rather than crystal clear ice. These layers of thin ice can be attached to the lake shore or stacked in multiple layers pushed on top of each other by wind (Figure 1). Depending on the thickness and appearance of the layer the translucent ice can blur features on the lake bottom or completely obscure them. The edge of the lake shore ice in Figure 1 casts a shadow on the lake bottom.

Advancing our understanding of the hydrological system on the surface of the GrIS requires observational knowledge on a range of scales with varying spatial and temporal resolution and coverage. On an ice-sheet-wide scale relevant parameters such as lake distribution and size can be best studied from spaceborne sensors, often providing high temporal resolution and year-round coverage that are important for the formation of the lakes. Process-related studies, however, generally require high-resolution observations over regional scales spanning hundreds of kilometers. While the resolution of spaceborne imaging is continually increasing, airborne imaging can provide complementary information at even higher resolution, often combining multiple sensors with coincident data acquisition.

The approaches most commonly used to derive bathymetry of supraglacial lakes on the GrIS make use of satellite imagery, mainly driven by spatial and temporal coverage of satellite imagery and its availability. These methods often use relationships between water depth and reflectance from natural color or multi-spectral imagery. For a recent summary of these remote sensing methods see Man et al. (2025). With the availability of ICESat-2 green (532 nm) satellite lidar data bathymetry

https://doi.org/10.5194/egusphere-2026-4143
Preprint. Discussion started: 17 August 2026

has been derived along ICESat-2 tracks and also used to calibrate and validate the image based methods (e.g., Arndt and Fricker, 2024; Datta and Wouters, 2021; Fair et al., 2020).

While space-based approaches have the advantage of ice-sheet wide coverage and long time series, they are limited in the spatial detail they can provide. Aerial imagery, which is often acquired together with data from other sensors, has the potential to increase the spatial resolution of our knowledge of the hydrological system of the GrIS. The use of aerial imagery has been expanded in recent years to derive shallow water and coastal bathymetry (e.g., Dietrich, 2017; Fuchs et al., 2024; Palaseanu-Lovejoy et al., 2023; Slocum et al., 2019; Woodget et al., 2015). Here we evaluate the applicability of two different approaches to derive supraglacial lake bathymetry using optical aerial images: Structure from Motion (SfM) and stereophotogrammetry. Both are widely used established techniques to create digital elevation models (DEMs) from images and have fundamental differences in their respective approaches. In general, SfM uses multiple overlapping images and iterative bundle adjustment that solves and optimizes camera positions and parameters (extrinsic and intrinsic) and the DEM. Stereophotogrammetry, on the other hand, typically requires highly accurate camera geometry and calibration.

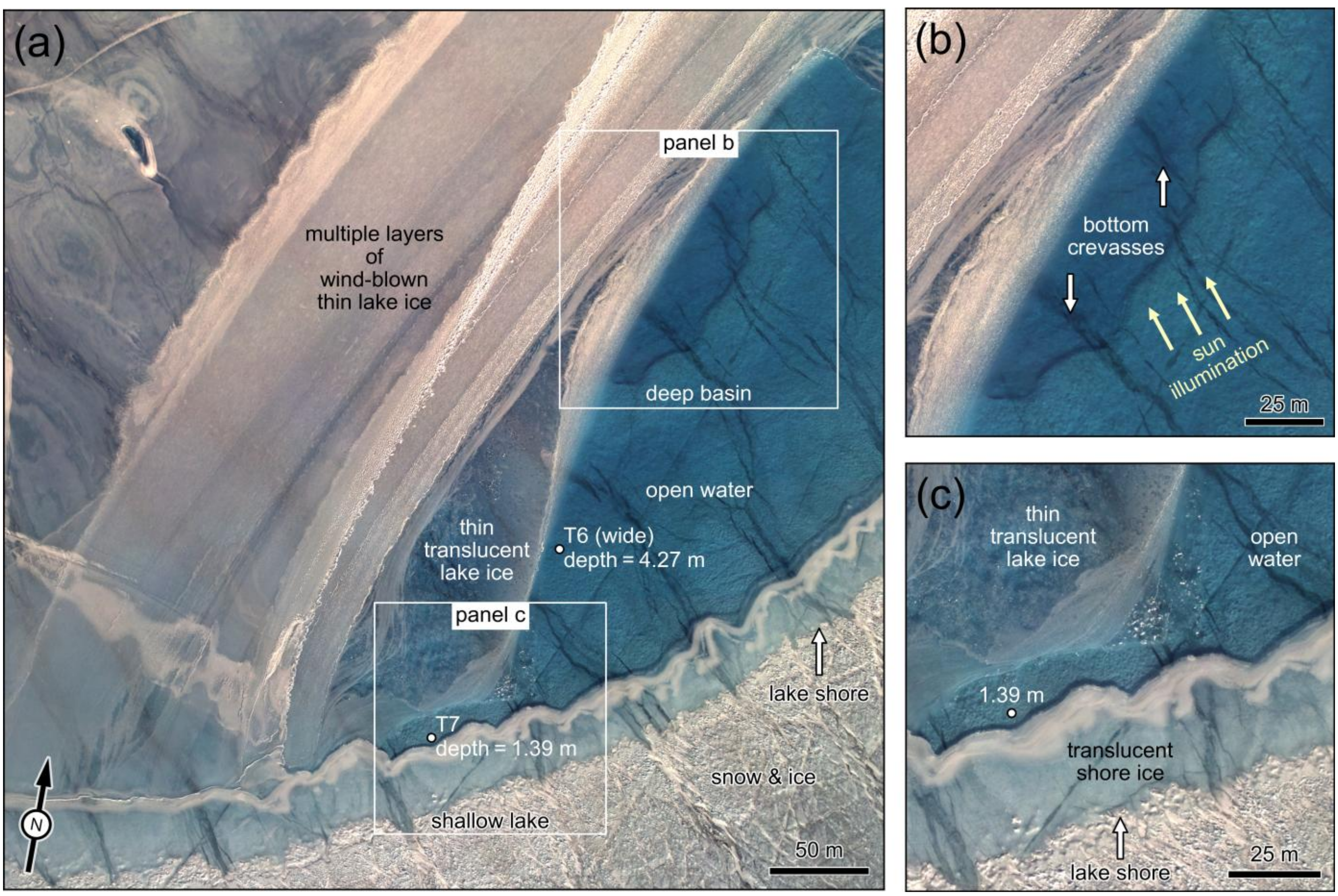

https://doi.org/10.5194/egusphere-2026-4143
Preprint. Discussion started: 17 August 2026

Figure 1: Characteristic features of supraglacial lakes visible in high-resolution (10×10 cm), natural color (red, green, blue; RGB), nadir-looking aerial imagery. The image of a partially ice-covered supraglacial lake in coastal northwest Greenland was taken with ATM's CAMBOT (Continuous Airborne Mapping By Optical Translator) camera system on September 6, 2019 and is available as a geolocated data product from NSIDC (Studinger and Harbeck, 2019). Two water depth point measurements from the ATM T6 and T7 lidars are marked by circles. Features labeled in the three panels are discussed in the text. For location of the lake see Figure 2b.

Natural-color aerial imagery has long been acquired over the GrIS as part of NASA's Operation IceBridge and is freely available as mission data products (MacGregor et al., 2021). Previous work has used the Ames Stereo Pipeline (ASP) to produce orthorectified images (Alexandrov et al., 2018a) and photogrammetric DEMs (Alexandrov et al., 2018b) that are aligned to coincident lidar data and did not include bathymetric processing. Here we use a camera system from NASA's Airborne Topographic Mapper instrument suite (ATM) for our analysis. To our knowledge this is the first time aerial images are being used to derive bathymetry of supraglacial lakes of the GrIS. We also have a unique opportunity to compare the image-based bathymetry with coincident topobathymetric data (Studinger et al., 2022a). We have selected two lakes for our analysis that have good lidar coverage, are among the deepest lakes in our data and also show limitations inherited in the methods we use. We refer to the two lakes as Lake CW (central west) for the lake shown in Figure 2a and Lake NW (northwest) for the lake in Figure 2b. Lake CW is located in the catchment of Sermeq Kujalleq (Jakobshavn Isbræ) and close to lake L1 (Figure 2a) discussed in Wehrlé et al. (2026). The drainage of this lake, 24 km southeast of the May 2019 terminus position, has affected the flow of Sermeq Kujalleq (Wehrlé et al., 2026). Lake CW discussed here is only 14 km away from the May 2019 terminus and appears to be approximately twice as large in satellite imagery from May 9, 2019 (Figure 2) suggesting its relevance for modulating ice flow within the fastest flowing ice stream in the GrIS.

https://doi.org/10.5194/egusphere-2026-4143
Preprint. Discussion started: 17 August 2026

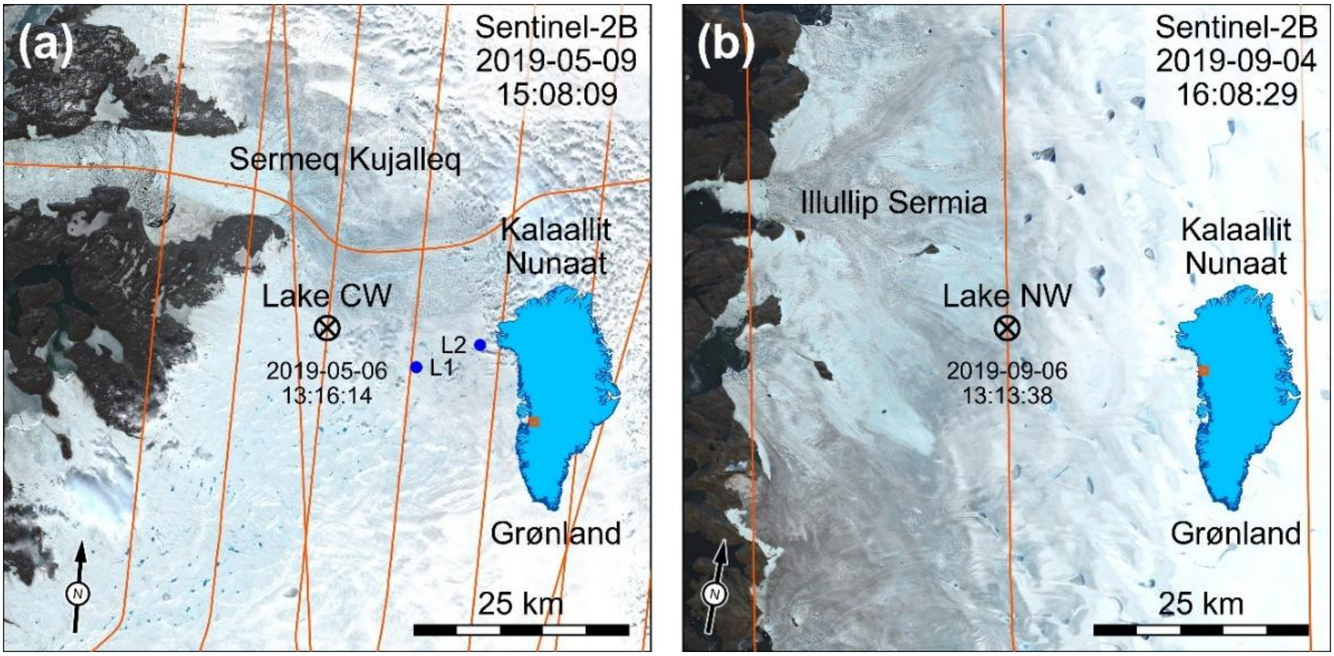

Figure 2: Locations of the two supraglacial lakes discussed in this paper on Sentinel-2B Level 2A surface reflectance, atmospherically corrected using bands 4, 3, and 2 (European Space Agency (ESA), 2025). Both composite RGB images span 75×75 km. Aircraft trajectories are shown in red with the location of the lakes marked by black crosses and time of the aircraft overpass. Locations of supraglacial lakes (black circle-and-cross symbol) in the catchment of Sermeq Kujalleq (Jakobshavn Isbræ) (a) and over a small tributary of Illullip Sermia (b). Red squares in index maps show the location and extent of the main maps. Glacier names are from Bjørk et al. (2015). We refer to the two lakes as Lake CW (central west, 49° 28' 45" W, 69° 1' 41" N) for the lake shown in (a) and Lake NW (northwest, 55° 4' 27" W, 74° 18' 56" N) for the lake in (b). The blue circles in (a) mark the locations the two supraglacial lakes L1 (49° 12' 50" W, 68° 59' 41" N) and L2 (49° 2' 8" W, 69° 1' 21" N) from Wehrlé et al. (2026).

2 Instruments and data sets

We use data from NASA's Operation IceBridge (OIB) from two campaigns flown over Greenland: one with the P-3 aircraft (N426NA) in June 2019 and one with the NASA Gulfstream G-V (N95NA) in September 2019. The airborne data products used here were part of NASA's Airborne Topographic Mapper instrument suite (ATM) and are freely available mission data distributed by the National Snow and Ice Data Center (NSIDC, https://nsidc.org/data/icebridge/data) and through NASA's Earthdata portal (https://www.earthdata.nasa.gov). Data products are distributed together with comprehensive instrument and data product documentation and have been described previously (MacGregor et al., 2021; Studinger et al., 2022a, 2024). Here we provide only a brief overview of the instruments and products relevant to this work and focus on the specific processing steps needed for existing data products for estimating bathymetry and some specific instrument calibrations that are required for our approach.

Among OIB's main goals over land ice were measuring ice surface elevation and change and determining ice thickness (MacGregor et al., 2021). Campaign timing was optimized to capture annual and seasonal variations in surface elevation and to maximize radar penetration. Greenland spring campaigns were typically flown between March and June, prior

https://doi.org/10.5194/egusphere-2026-4143
Preprint. Discussion started: 17 August 2026

to the main onset of summer melt. Seasonal campaigns were conducted in the fall after the melt season, around September, when parts of the surface began to refreeze and lakes became covered with thin ice (Figure 1) making bathymetry estimates from the air a challenge (Studinger et al., 2022a). Figure in the Appendix shows the surface temperature over the duration of the two campaigns together with melt indicators at the two lake locations. An overview of the two campaigns including a discussion of the presence of surface water is given by Studinger et al. (2022a). Another limitation imposed by the survey design is image acquisition along flight lines. Typically, SfM requires overlapping images of the same features on the ground from different flight directions and elevations for accurate DEM calculation (e.g., Fuchs et al., 2024). However, having accurate position and attitude information of the camera sensor can mitigate that limitation as discussed later.

2.1 Merging position and attitude data for camera pose

To use the highest available accuracy position and attitude data for determining the camera pose (i.e., the position and orientation of the camera) we combine three navigation data streams that all contain the Global Positioning System (GPS) time as the common reference for synchronization: 1) 10 Hz GITAR (GPS Inferred Trajectories for Aircraft and Rockets), 2) 200 Hz SBET (Smoothed Best Estimate of Trajectory), and 3) 2 Hz ATM's auxiliary (AUX) data that are distributed together with the Level 1B geolocated IOCAM1B data product (Studinger and Harbeck, 2019).

Figure 3 shows a generalized diagram of the processing steps involved in creating input data for subsequent image processing. The GITAR trajectories are derived from double-differenced GPS measurements (DGPS) between the aircraft and multiple, precisely located ground stations that are operated during a campaign (Martin et al., 2012). GITAR uses atmospheric reanalysis models from the National Center for Environmental Prediction (NCEP) for correction of tropospheric propagation effects on ranges to satellites instead of a commonly used world-wide standard atmosphere model (Saha et al., 2010). In addition, GITAR estimates scale factor corrections for the aircraft and ground stations and can process extremely long GPS baselines required for polar research (i.e., South America to Antarctica). GPS antenna phase center positions, including installation-specific phase center offsets of aircraft-mounted GPS antennas, are calculated at 10 Hz.

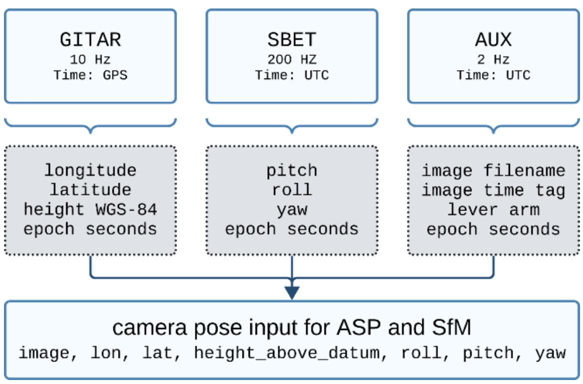

Figure 3: Diagram of processing flow for merging three navigation data streams into camera pose for input into ASP and SfM.

The SBET data stream contains processed 200 Hz trajectory data from an Applanix 610 POS AV GPS/IMU sensor and POSPac package, including attitude (pitch, roll, yaw). The AUX data stream contains intervalometer trigger event times for the camera's shutter. A Javad Delta/Sigma GPS receiver was programmed to generate the 2 Hz intervalometer hardware trigger to the camera. The trigger pulses are perfectly synchronous with the GPS raw data measurements to be postprocessed. We use the 10 Hz GITAR position trajectory and 200 Hz SBET data streams to interpolate position and attitude data at the 2 Hz camera shutter trigger times. We replaced the 200 Hz POSPac positions with 200 Hz interpolated 10 Hz GITAR positions as the GITAR positions are more refined and accurate. We then use the lever arm between the GPS antenna phase center and the camera's sensor, that is included in the header of the AUX data files, to calculate the pose of the camera sensor. The merged trajectory data used in this paper are published in a separate archive (Studinger et al., 2026b). A repository with code and tutorials for how to merge the three data streams and calculate sensor positions is part of this paper (Studinger et al., 2026a).

2.2 Natural-color optical imagery

The nadir-looking, three-channel (red, green, and blue, RGB) digital camera is an Allied Vision Prosilica® GT4905 C with a digital global shutter and a Zeiss® Distagon 28 mm f/2 ZF.2 lens. The image sensor has 4896 × 3264 pixels with a pixel size of 5.5 µm × 5.5 µm (Allied Vision, 2022). OIB surveys were typically flown at a draped elevation of around 460 m above ground level resulting in a pixel size of around 9 cm on the ground (MacGregor et al., 2021). The camera shutter is triggered by a two pulse per second (PPS) signal from a Javad Delta/Sigma GPS receiver for accurate timing. The latency between the intervalometer trigger signal and the camera's shutter trigger time is estimated using calibration flights over survey targets on airport ramps (Studinger and Harbeck, 2019). OIB flights are typically flown at a ground speed of 140 m s^{-1}, resulting in an 80% overlap between consecutive images acquired at 2 Hz (MacGregor et al., 2021). On average the same feature on the ground is imaged in five consecutive images from different perspectives. The camera system is a passive sensor that depends on varying natural sunlight for illumination. An operator adjusts camera parameters based on conditions during the flight to optimize image quality and exposure (Studinger et al., 2022a, 2024; Studinger and Harbeck, 2019, 2020). The two image data products we use here with NSIDC data set identifiers IOCAM0 and IOCAM1B are not radiometrically calibrated (Studinger and Harbeck, 2019, 2020).

2.3 Lidars

The primary instruments in the ATM instrument suite were two small-footprint, short-pulsed, topobathymetric lidars operating at 532 nm and 10 kHz (MacGregor et al., 2021; Studinger et al., 2022a, 2024). The short pulse width of 1.3 ns, 64 cm footprint and high spatial point density makes this data set ideal for comparing bathymetry estimates between the three methods discussed in this paper. Both are conically scanning lidars with the wide scanner T6 having an off-nadir angle of 15° and the narrow scanner T7 of 2.5°, resulting in an approximate swath width of 245 and 40 m, respectively. There is no mission bathymetry data product, however the methodology to use the ATM waveform products ILATMW1B and ILNSAW1B

https://doi.org/10.5194/egusphere-2026-4143
Preprint. Discussion started: 17 August 2026

(Studinger, 2018a, b) to estimate bathymetry over supraglacial lakes has been previously published (Studinger et al., 2022a) together with the code (Studinger, 2022).

3 Methods

We use two image-based methods, traditional stereophotogrammetry and structure from motion (SfM), to determine shallow-water bathymetry over supraglacial lakes and compare the results with coincident topobathymetric lidar data. For stereophotogrammetry processing we use the NASA Ames Stereo Pipeline (ASP), a powerful open-source toolbox with a long legacy, a broad user community, and active tool development (Alexandrov et al., 2026; Beyer et al., 2018). We use a commercial implementation, Agisoft Metashape, for SfM processing. The simultaneous acquisition of aerial photography, suitable for photogrammetry applications, and topobathymetric lidar is rare. Figure 4 shows the concept of simultaneous data acquisition on a single airborne platform surveying the same scene on the ground.

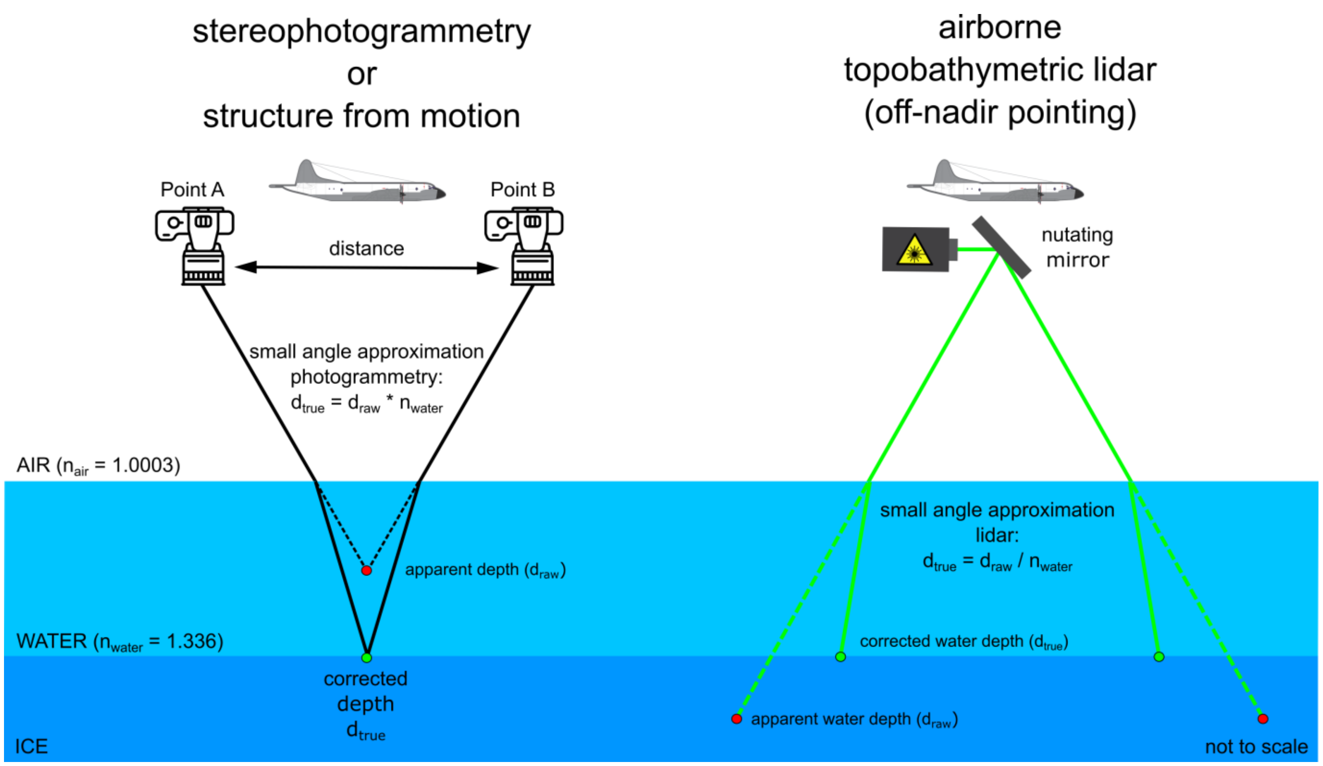

Figure 4: Conceptual drawing of simultaneous airborne photo and lidar acquisition on the same platform with image-based (left) and lidar-based (right) bathymetry estimates. The field of view (FOV) of the camera slightly exceeds the swath width of the lidar on the surface (245 m) and provides full coverage. The time between image acquisitions when the aircraft moves from Point A to Point B is 0.5 seconds, resulting in an approximate 80% overlap between images.

https://doi.org/10.5194/egusphere-2026-4143
Preprint. Discussion started: 17 August 2026

For the image-based methods a nadir-looking camera on the aircraft takes pictures of the ground with sufficient overlap between consecutive images while a topobathymetric lidar images the same area at the same time. At a nominal ground speed of 140 m s^{-1} the distance between two images taken 0.5 s apart is 70 m. The image-based methods operate in the spatial domain, whereas the lidar-based method relies on time-of-flight measurements in the time domain. As a result, the uncorrected depth d_{raw} of the image-based methods is biased towards shallower depths. Using a rule of thumb valid for small angles (e.g., Woodget et al., 2015) the approximate corrected depth is $d_{true} = d_{raw} * n_{water}$, where n_{water} is the refractive index of water (Figure 4). For the lidar, the corrected depth $d_{true} = d_{raw} / n_{water}$. For our bathymetric processing we use different approaches for each method that accurately account for refraction in water and are discussed in Section 3.6. We begin with a description of preprocessing of data products to create input required for both methods.

3.1 Surface classification and automated lake detection

Estimating water depths from stereophotogrammetry or SfM requires knowledge of the surface type (water or land/ice) for each image pixel. Each processed image requires a surface classification image of the same size and resolution as the original image that acts as lake mask for bathymetric processing accounting for refraction in water. We use two different approaches and discuss their pros and cons. The first method is using the Normalized Difference Water Index modified for ice ($NDWI_{ice}$) calculated from the red and blue channels: $NDWI_{ice}$ = (blue – red)/(blue + red). $NDWI_{ice}$ increases the spectral contrast between water and ice (e.g., Yang and Smith, 2013). This approach has been previously applied to the 2019 spring campaign using a single empirical threshold to separate water pixels from snow and ice (Studinger et al., 2022a). While the approach is robust it can also produce occasional false detections as discussed in Studinger et al. (2022a). Here, we use a modified version of this approach that determines the $NDWI_{ice}$ threshold between water and ice for each image using Otsu's (1979) method that was expanded to allow for multiple thresholds (Liao et al., 2001). The application of the method to images over the lake flown on May 6, 2019 (Figure 2b) together with the code is available as tutorial (Studinger et al., 2026a, Surface classification and automatic detection of supraglacial lakes). The approach of using an $NDWI_{ice}$ threshold was primarily designed to locate lakes and streams in tens of thousands of images and therefore needed to be computationally efficient. For photogrammetry applications each pixel in an image needs to be accurately classified so the surface type image can be used as a mask for bathymetric processing. The $NDWI_{ice}$ threshold approach fails when pixels have similar values that are not separated enough to be distinguished and belong to different surface types. This can be the case for newly formed thin, translucent lake ice as shown in Figure 1. Figure 1c shows an area with thin, translucent lake ice that looks very similar to the area with open water next to it. The only visual indication of a thin ice cover are blurred features at the lake bottom, like crevasses, that are much clearer in the area with open water. For situations like this we use an approach that connects pixels and identifies areas and can be used for image segmentation. We use the open-source Segment Anything Model (SAM) that is available as a Python module together with the training data (Kirillov et al., 2023). A demonstration of using SAM to identify coherent areas of open water together with the code is available as a tutorial (Studinger et al., 2026a, Supraglacial lake detection with the AI-based Segment Anything Model (SAM)). As shown in the tutorial, the SAM algorithm can have difficulties tracking shallow water

https://doi.org/10.5194/egusphere-2026-4143
Preprint. Discussion started: 17 August 2026

depths near shorelines. It performed well though for reliably creating a lake mask of open water pixels of the lake shown in Figure 1 while excluding the thin ice and other areas from the lake mask. We combine both approaches to first quickly identify lakes in images and if needed refine the lake mask using the slower SAM image segmentation. To create so-called prompts for SAM we first determine coherent regions in the $NDWI_{ice}$ image mask using a connected component analysis approach. We then use the centroid locations of the identified regions as input/prompts for SAM to seed image segmentation (Studinger et al., 2026a, Surface classification and automatic detection of supraglacial lakes).

3.2 Conversion of natural-color images to luminance

Stereophotogrammetry and SfM processing tools generally require single-channel grayscale (luminance) images. There are several ways to convert natural-color (RGB) images to luminance images for bathymetric processing that we will briefly discuss here. A commonly used approach is to use weighted luminance relationships between red, green and blue channels for conversion into gray scale. Varying implementations of this approach are readily available in open source software libraries like Pillow (Murray et al., 2026) or OpenCV (Bradski, 2000). However, penetration of light into water depends on its wavelength. In general penetration increases from red, to green, to blue (e.g., Purkis and Klemas, 2011, Fig. 8.8). When separated into red, green and blue bands, supraglacial lake images show increasing detail in the lake bottom from red, to green, to blue. We have demonstrated this effect in a tutorial together with the code to convert RGB images to luminance (Studinger et al., 2026a, Conversion of natural-color (RGB) images to single-channel grayscale (luminance) images for bathymetric applications). While providing good penetration, the green channel also shows good contrast between water and ice. We therefore use the luminance of the green channel for input into ASP processing for images of supraglacial lakes. The situation is different for lidar and camera calibration flights. The flights are typically conducted over surveyed airfield aprons/ramps, which are often located in vegetated areas. Here, the red or near infrared bands typically show higher clarity and detail compared to the green and blue bands. An example of this effect is also shown in the tutorial (Studinger et al., 2026a, Conversion of natural-color (RGB) images to single-channel grayscale (luminance) images for bathymetric applications). The conversion within Agisoft's Metashape is done internally and details are not publicly available.

3.3 Camera calibration

To map image pixels captured with the camera's sensor to locations on the earth's surface requires accurate knowledge of the camera system's intrinsic optical parameters and extrinsic pose parameters. These parameters are used in transformation matrices that convert pixels from sensor coordinates to the camera coordinate system and eventually to a geodetic world coordinate system that locates pixel locations on the surface of the earth. Before each campaign the camera system is calibrated using repeat passes over airport ramps flown at different altitudes and orientations. For each campaign we typically use approximately 20 ground control points (GCPs) on the ramps. These are prominent easily identifiable features, such as intersections of apron markings and runway lights, that can be identified in image pixels. We determine the locations of these features with survey grade DGPS with an accuracy of a few centimeters. The GCP's are used to determine the camera's lens

https://doi.org/10.5194/egusphere-2026-4143
Preprint. Discussion started: 17 August 2026

distortion parameters and focal length and refine sensor mounting biases in the lever arm between the GPS antennas' phase center and sensor plane as well as and pitch, roll, and yaw angles between the IMU and the camera sensor (Studinger and Harbeck, 2019). For the two campaigns discussed here we use the built-in methods in Metashape to determine a set of parameters consistent with the GCPs. The details of the Metashape approach are not publicly available. ASP has similar capabilities with the `camera_solve` tool using GCPs to optimize the camera's intrinsic and extrinsic parameters and create pinhole camera models. We use Metashape's camera calibration as consistent input for both SfM and ASP. We then apply the refined mounting biases to the trajectory data and create camera model files described in the next section.

3.4 Stereophotogrammetry

Stereophotogrammetry determines the geolocated relief of a surface on the ground from two overlapping images with different perspectives of the same terrain (e.g., Beyer et al., 2018). The technique requires accurate knowledge of the camera's position and pose (extrinsic parameters) and the camera's optical parameters, referred to as intrinsic parameters. For stereographic processing with ASP, we begin with the output from the navigation processing shown in Figure 3, together with the pinhole camera model file as input into ASP's `cam_gen` program (Figure 5). The `cam_gen` program uses the geodetic coordinates and attitude angles, i.e., extrinsic parameters. These are combined with the camera's intrinsic parameters like optical center, focal length, lens distortion and pixel pitch, to generate a pinhole camera model for each image based on the sensor position and orientation at the time of acquisition. The information is stored in ASP's `.tsai` text format and referred to as a camera model (Tsai, 1987). To have a self-consistent set of camera models as input for stereo processing the model parameters can be refined in a process called bundle adjustment. ASP's `bundle_adjust` tool (Beyer et al., 2018) is based on the Ceres least square solver (Agarwal et al., 2023) and minimizes errors in camera pose. The outputs are refined camera model files for each image in a sequence of images. Given the high quality of our position and attitude input data we find the effect of bundle adjustment small, however, it can be a critical processing step for other applications.

https://doi.org/10.5194/egusphere-2026-4143
Preprint. Discussion started: 17 August 2026

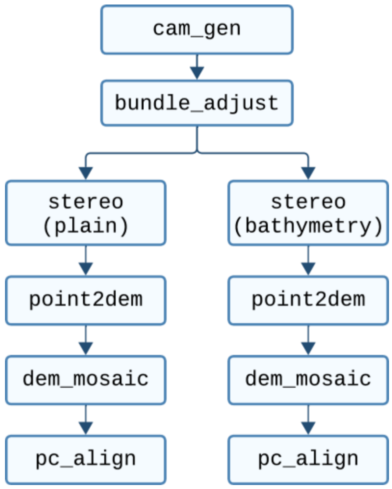

Figure 5: Diagram of ASP processing flow. To allow a direct comparison with SfM we process the images without ASP's bathymetry module (plain) and with the bathymetry module for pixels that have been classified as open water.

The bundle adjusted camera models and gray-scale images of the green channel luminance are then processed with ASP's `parallel_stereo` module, which combines a sequence of processing steps (Alexandrov et al., 2026; Beyer et al., 2018) that we briefly summarize. A fundamental first step in stereophotogrammetry processing is to locate interest points or features in both images of an image pair through image correlation. We use ASP's OpenCV implementation of the Scale-Invariant Feature Transform (SIFT) algorithm for sparse detection (Bradski, 2000). The shifts in matched pixel coordinates between the two images are called disparities and are a function of parallax and therefore related to pixel height. The outputs are aligned and normalized image pairs that are used as input into a denser image correlation in the stereo alignment stage with ASP's implementation of the More Global Matching (MGM) algorithm (Facciolo et al., 2015), that is suitable for textureless regions like ice sheets. The resulting map of disparities is then refined on a subpixel level using ASP's subpixel mode 2, which is best in terms of quality and most costly in terms of computation time. The next step is to convert disparities into a 3-D point cloud by triangulating intersecting rays from the two camera poses. The distance between the two intersecting rays is called the triangulation error and can be interpreted as a relative measurement for the quality of the stereo processing (Beyer et al., 2018). In our processing the triangulation error is typically on the order of a few centimeters and below the size of an image pixel suggesting reliable processing results. The next step is to produce a gridded terrain model (DEM) from the point cloud, which is done by ASP's `point2dem` program (Figure 5). Since stereo processing can only be done on image pairs the resulting DEMs for the overlapping parts of the two images need to be merged into a single seamless DEM using ASP's `dem_mosaic` command line tool. As an optional last step, the DEM's height and location can be refined by aligning it with an existing reliable DEM or a point cloud of the region. In our case these are the elevations from our airborne lidar. However, we find that the improvements are marginal because of the high quality of our camera models. The ASP program that aligns a DEM or point cloud relative to another is called `pc_align`.

One aspect that needs to be considered for stereo processing that is different for SfM, is a requirement for the so-called convergence angle. The convergence angle is defined as the angle between the two rays from consecutive images of the same feature on the ground. In general, small convergence angles result in good horizontal accuracy and lead to weaker constraints on vertical reconstruction. Vice versa, larger convergence angles strengthen vertical accuracy and reduce accuracy in the horizontal component. For ASP stereo processing convergence angles should be between 15° and 40°. ASP calculates convergence angles as part of the bundle adjustment. For images taken 0.5 seconds apart most of the overlapping area between two images (75%) is below the 15° lower threshold resulting in significant vertical noise in the DEMs. The convergence angle increases with time and distance between images at the expense of reducing the area of overlap between the two images. For images taken 1.0 seconds apart we have sufficient overlap between the images to create a seamless DEM from a sequence of images with convergence angles of 15° and good vertical reconstruction. We therefore use only image pairs that are 1.0 seconds apart for stereo processing.

3.5 SfM

We use a commercial implementation, Agisoft Metashape, for SfM processing. The processing follows a multi-step approach that tightly integrates post-processed GNSS trajectories, pre-computed camera focal lengths, and lens distortion and orientation calibrations. Even with precise post-processed DGPS/IMU data, initial SfM processing can exhibit significant surface tilts and elevation offsets for image sequences collected along a straight flight line with no lateral overlap (e.g., Fuchs et al., 2024). The SfM process is sensitive to minor trajectory inaccuracies and variations in the camera sensor and lens caused by temperature and pressure differences between calibration and data collection. These manifest primarily as changes in focal length and image sensor pixel positioning. To resolve this, concurrent ATM lidar data (T6 & T7) is used to physically calibrate and anchor the SfM data. By iteratively comparing the uncorrected SfM Digital Elevation Model (DEM) with lidar point clouds, precise IMU mounting biases are identified. Adjusting pitch and roll references removes along-track tilt, aligning the SfM elevation offset with true lidar elevations over non-submerged portions. Small adjustments to the camera focal length may also be required for optimal alignment. We use the refined parameters for both SfM and ASP processing to have consistent data for direct comparison of the methods.

3.6 Refraction correction

Both image and lidar-based approaches need to account for the change in refractive index from air to water by correcting the initial apparent depth (Figure 4). Conventional stereophotogrammetry triangulates rays from an image pair. Therefore, underwater stereo triangulation can be directly calculated resulting in correct water depths (e.g., Dietrich, 2017; Alexandrov et al., 2026). This approach is implemented in the ASP bathymetry module that is part of the `parallel_stereo` module (Palaseanu-Lovejoy et al., 2023). Refraction correction for SfM is different from the correction applied to stereo processing. SfM uses multiple overlapping images and iterative bundle adjustment that solves and optimizes camera positions and parameters. Therefore, the depth correction is an iterative process. To correct SfM-derived water depths we use an iterative

https://doi.org/10.5194/egusphere-2026-4143
Preprint. Discussion started: 17 August 2026

method developed for shallow water bathymetry (Dietrich, 2017) that is implemented in the pyBathySfM module (Dietrich, 2026) and can be applied to DEMs created from SfM that include water bodies. A similar approach was developed by Fuchs et al. (2024) and applied to melt ponds over sea ice. The refractive index of water varies with wavelength, temperature, and salinity. We use empirical relationships from Dietrich and Parish (2025) to calculate the refractive index at 532 nm. We assume the temperature of the water to be close to 0.0°C with a salinity of freshwater of S = 0.1 PSU (practical salinity units). The refractive index in water at 532 nm is then n_{water} = 1.336 for the laser. The camera sensor of the green channel, which we use for lakes as discussed later, has its maximum efficiency near 530 nm. We therefore use the same refractive index n_{water} for both the camera and lidar data. For air we use a refractive index of n_{air} = 1.0003, a value commonly used for the standard atmosphere. Both methods require accurate water surface elevations. Ideally, we would use the water surface elevation from lidar data since it is the most reliable and accurate elevation measurement of the water surface we have. However, other methods exist to determine the water surface elevation without lidar data (e.g., Dietrich, 2017; Fuchs et al., 2024; Palaseanu-Lovejoy et al., 2023) and as discussed in the next section we have to revert to these methods in our work because of differential penetration of green laser light into snow and ice over Lake NW.

4 Results

To directly compare the results from SfM and ASP we first use DEMs produced without bathymetric correction, referred to as plain processing, since the two different approaches for refraction correction could introduce differences only related to the specific method and not the general approaches. We compare the elevation differences between the image-based bathymetry methods and the lidar and discuss potential biases.

4.1 Lake NW

Lake NW (Figure 1 and Figure 2) shows a variety of features relevant for bathymetry estimates: the lake is partially covered by newly formed layers of thin lake ice that have been pushed on top of each other by wind (Figure 1a). The milky texture of this ice obscures features at the lake bottom and therefore prevents bathymetry estimates from both lidar and optical imagery. Along the shoreline a layer of translucent shore ice is thin enough for a blurred view of lake bottom features such as crevasses. The shadow of this band of thin ice on the lake bottom confirms that this ice is floating on the lake surface (Figure 1c). The lake area with open water reveals clear views of features on the lake bottom because of the very low turbidity of the water, making it ideal for bathymetry estimates. The change in blue color in the RGB image reflects a change in water depth with darker blue representing deeper depths. The lake bottom shows several deep bottom crevasses with the darkest blue. The sun illumination during the overpass is subparallel to the orientations of the crevasses.

https://doi.org/10.5194/egusphere-2026-4143
Preprint. Discussion started: 17 August 2026

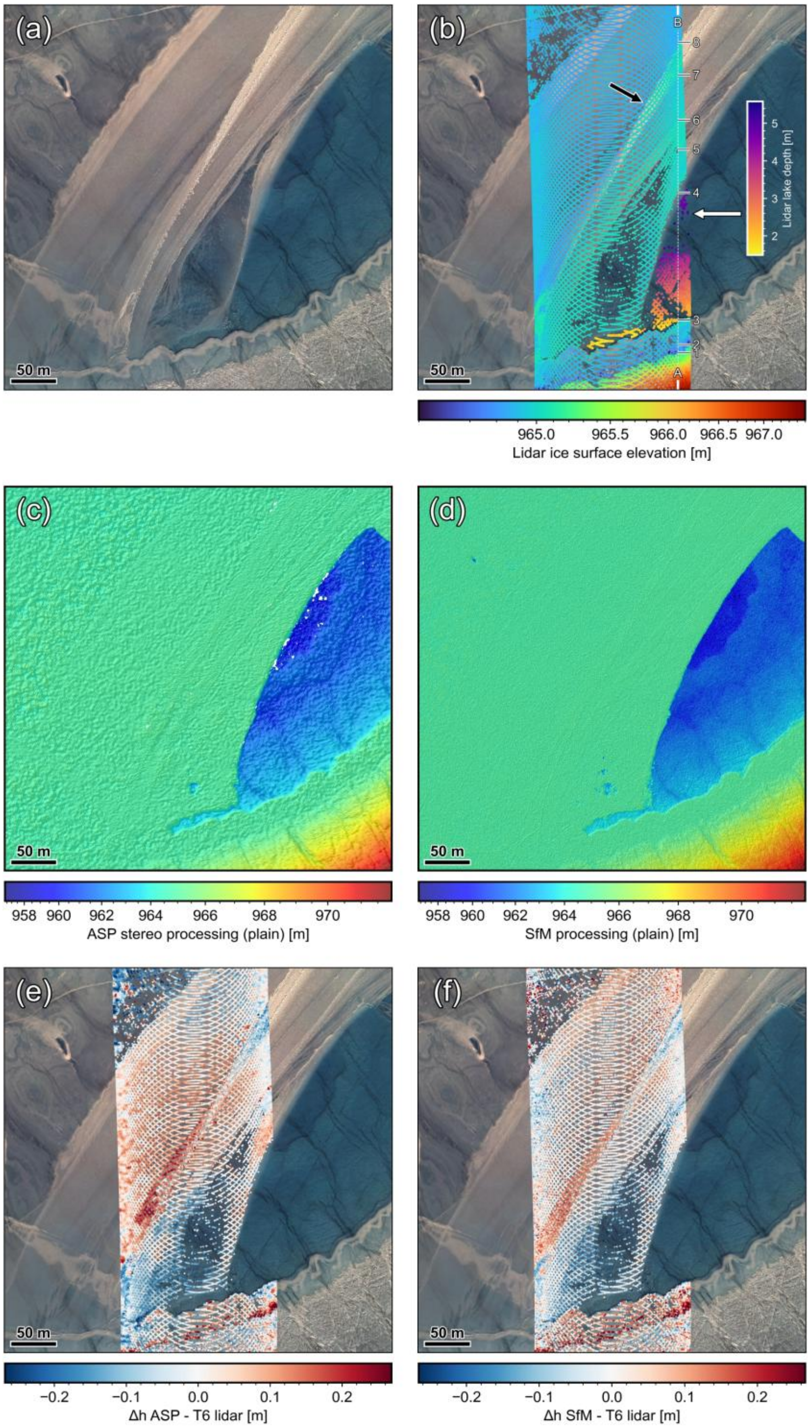

Figure 6: Lake NW stereo and SfM results without refraction correction (plain). For location of the lake see Figure 2b. (a) Natural color mosaic. (b) Lidar point cloud and lidar-derived bathymetry with location of profile shown in Figure 7. (c) DEM from stereo processing. (d) DEM from SfM processing. (e) Elevation difference Δh between stereo DEM and lidar point cloud and same for SfM (f). A version of Figure 6 using color vision deficiency (CVD)-friendly color palettes for panels (b), (c), and (d) is provided in Figure A2.

We can therefore rule out that these darker areas are shadows. The darker areas, however, could also represent cryoconite, a dark sediment at the bottom of supraglacial lakes that mainly consist of small mineral particles (dust, soot, volcanic ash), organic matter (algae, etc.), and black carbon, which seems not to be the case here. Shadowing from the low angle sun illumination (azimuth: 141.57° E, altitude: 18.92° at the time of overpass) reveals small features that reflect the surface roughness of the lake bottom (Figure 1).

4.1.1 Lidar-derived bathymetry and differential penetration at 532 nm at Lake NW

Lidar-derived water depths of supraglacial lakes can be biased because green (532 nm) laser light not only penetrates water, it can also penetrate clear ice. Differential penetration is the variation in how deeply green laser light penetrates and scatters within the bulk volume of thin ice versus snow or open water. Differential penetration into ice can cause range and subsequently depth bias from subsurface volume scattering (e.g., Studinger et al., 2024; Smith et al., 2025, 2018; Fair et al., 2024). Penetration of the laser light into ice can be detected from broadening of the return laser pulse. There are several factors that can cause pulse broadening of the return waveform and therefore range biases. In general, the slope and roughness of the surface within the illuminated lidar footprint can broaden the return pulse (Brenner et al., 2012; e.g., Studinger et al., 2024). Pulse broadening caused by surface slope and roughness is typically equally distributed in the leading edge and the tail and symmetric around the maximum of the pulse (Brenner et al., 2012; Studinger et al., 2024; Smith et al., 2018; Fair et al., 2024; Smith et al., 2025). Because of its symmetry around the maximum, it does not cause range biases when commonly used range trackers such as pulse centroids or Gaussian waveform fitting are used, however, it can cause range biases for leading edge trackers though (Smith et al., 2018).

Over Lake NW, differential penetration manifests itself in two ways: subsurface penetration in layers in thin ice and subsurface penetration at the lake bottom. The first form is similar to observations over newly formed sea ice where the floating sea ice can appear several tens of cm below surrounding lidar measured water surface elevations, because of differential penetration into the thin ice (Studinger et al., 2024). The lidar elevation biases over thin ice over Lake NW can be seen in a profile near the edge of the swath with the highest lidar point density (Figure 6b). The elevation profile in Figure 7 shows the elevation of the open water above the biased elevation of the multiple layers of thin lake ice along the profile. Numbers along the profile mark the same features in profile and map view (Figure 6b, Figure 7). The return signal strength is indicative of changing reflectivity of the different features, primarily caused by surface roughness.

https://doi.org/10.5194/egusphere-2026-4143
Preprint. Discussion started: 17 August 2026

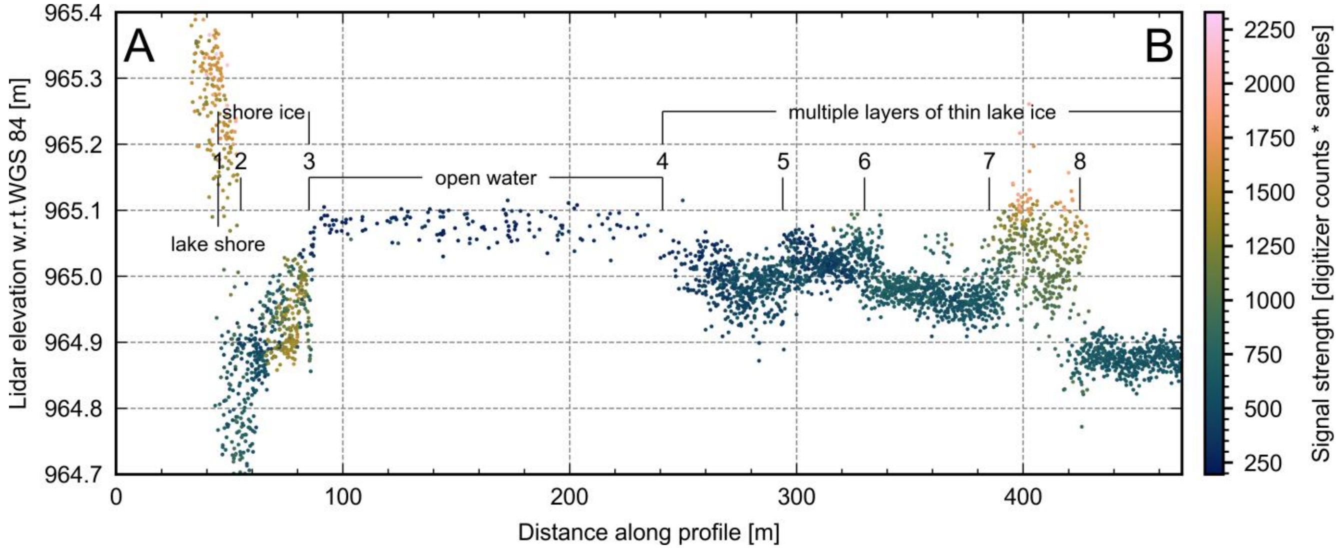

Figure 7: Profile of lidar elevations across Lake NW. For location of profile see Figure 6b. Numbers along the profile mark the same features in the profile and map view in Figure 6b.

The second form of differential penetration occurs at the lake bottom and to our knowledge has not been described yet in the literature. We have selected two lidar waveforms of the wide (T6) and narrow (T7) scanner over the shallow and deep parts of the lake (Figure 1a) and determined the pulse broadening of the waveforms using an approach we have previously developed (Studinger et al., 2024). To distinguish instrument-related pulse broadening from changes in pulse width and shape caused by geophysical interaction across a target surface we first determine the impulse response function (IRF) from laser footprints over a target with no penetration, and surface roughness or slope that can be neglected over the size of a lidar footprint. We stacked and normalized all return waveforms over the flat concrete surface of the ramp at Thule Air Base (now Pituffik Space Base) from a pass over the ramp on September 9, 2019, manually excluding off-ramp footprints and returns from aircraft and vehicles parked on the ramp based on georeferenced optical images (Figure). Figure 8 shows the pulse broadening at the water-ice interface at the lake bottom. The waveforms from the air-water interface do not show pulse broadening compared to the IRF from the ramp pass, meaning that the air-water elevations have no penetration-related bias. The pulse broadening determined from the pulse width of the water surface divided by the pulse width of the bottom return is 1.69 for both T6 and T7. This suggests that pulse broadening does not scale with water depth or angle of incident. We can therefore rule out detectable contributions from these two effects to the pulse width and shape observed over the lakes. This is consistent with the visual appearance of low turbidity in the optical images and hence low volume scattering within the water column. We have estimated the elevation bias resulting from differential penetration between -3 and -5 cm, however, this estimate is sensitive to how the IRF and lidar waveforms are aligned. It does reflect, however, a robust order of magnitude estimate and shows that the elevation bias at the lake bottom is much smaller than over the layers of thin ice on the surface. The varying changes in lidar elevation bias ranging from a few cm to several tens of cm over a short profile create challenges that we will discuss in the following sections.

https://doi.org/10.5194/egusphere-2026-4143
Preprint. Discussion started: 17 August 2026

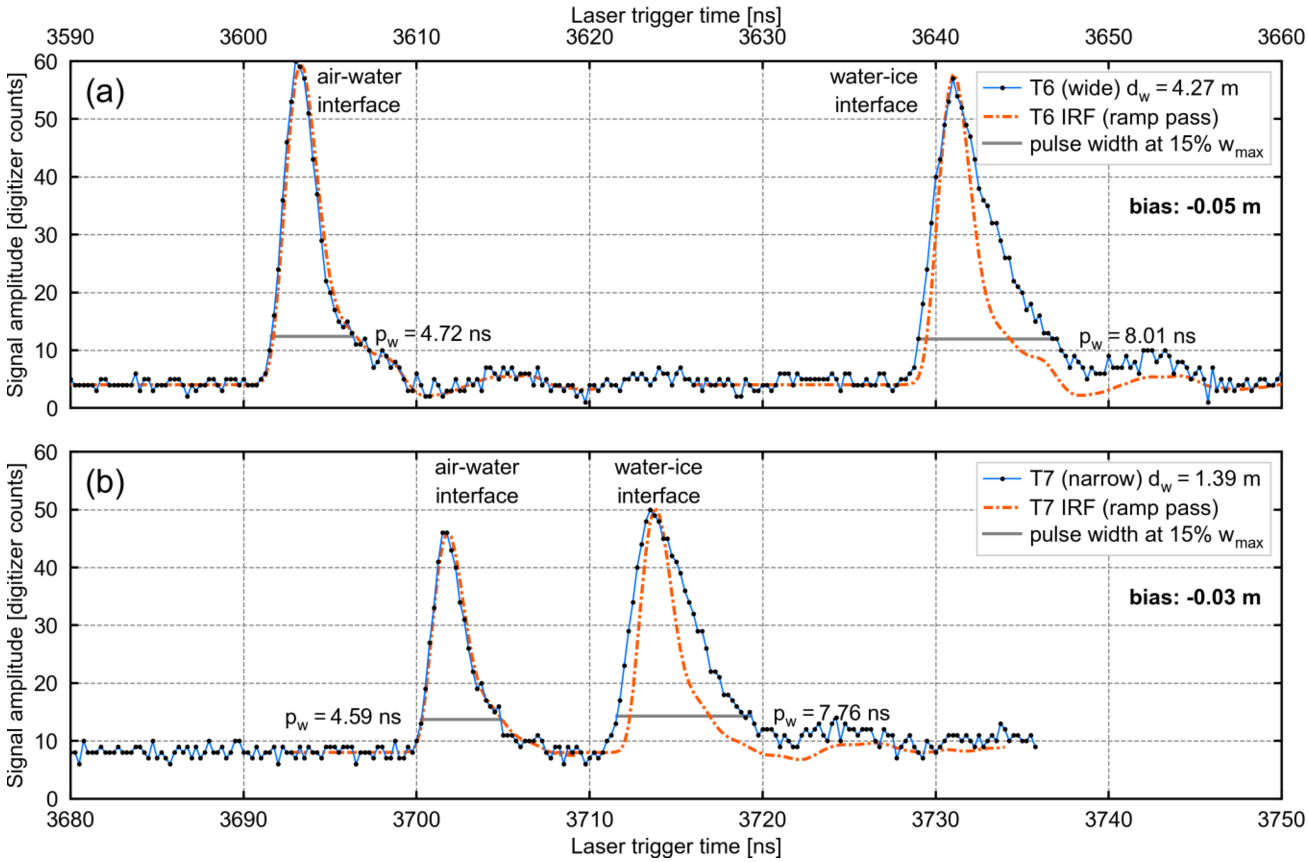

Figure 8: Pulse broadening of lidar waveforms caused by subsurface differential penetration of 532 nm light at the lake bottom (water-ice interface) of Lake NW. (a) T6 wide scanner. (b) T7 narrow scanner. For locations of waveforms see Figure 1.

4.1.2 Comparison of plain processing without refraction correction

To merge and blend the individual overlapping DEMs created from stereo point clouds we use the standard deviation of the vertical uncertainty determined for the stereo point cloud as inverse weights for each pixel. During DEM merging and blending with `dem_mosaic` pixels with larger convergence angles and therefore smaller vertical uncertainty are given more weight. This option, however, is not available in the bathymetry module. We use 9 images for the stereo processing that we process in 8 pairs with images 1.0 secs apart to maintain optimal convergence angles.

To facilitate a more direct comparison we have aligned both DEMs with the ice surface elevations from the T6 lidar (Figure 6b) excluding lidar points at the lake bottom and limiting horizontal displacement to 5.0 meters during the alignment. Because of the varying elevation biases in the lidar this is not ideal, but it makes the elevations from two DEMs comparable since both are referenced to the same data. For SfM processing the lidar point cloud was used to constrain DEM generation. The stereo DEM had a 25 cm elevation bias that was removed during alignment with no obvious tilt.

Figure 6 (c and d) show the plain DEMs without refraction correction. Both methods resolve features visible in the RGB image mosaic well; the stereo processing, however, has some small gaps over the deep basin. The hill shading applied

https://doi.org/10.5194/egusphere-2026-4143
Preprint. Discussion started: 17 August 2026

to the DEMs reveals subtle differences in surface texture between the two methods. SfM processing shows a slightly smoother surface compared to stereo processing. The subtle changes in surface roughness visible in both DEMs correlate with the bands of multiple thin ice layers. The stereo processing seems to resolve slightly more of that variation in surface roughness interpreted from the RGB imagery. The elevation difference Δh between the two DEMs and the lidar point cloud over snow and ice surfaces is 0.09 m (1-σ standard deviation) for both (Figure 6e, f). The stereo DEM appears to have smaller extremes (stereo: -0.70m, +0.57; SfM -1.72m, +0.95 m). The elevation differences show the expected random pattern which is overprinted by elevation changes that correlate with the visible bands of multiple thin ice layers. The reason for this is that the lidar elevations are biased over the bands because of differential penetration. The stereo and SfM methods using optical images are not sensitive to that.

The elevation difference Δh between the two DEMs is shown in Figure 9 and has a standard deviation of 0.21 m. When masked to water pixels only, the standard deviation increases to 0.26 m because the steeper lake-bottom topography amplifies elevation differences arising from small geolocation offsets. In contrast, restricting the analysis to the ice surface pixels outside the water surface yields a lower standard deviation of 0.18 m, consistent with the comparatively flat and homogeneous ice surface, where geolocation differences result in smaller elevation variations. Δh shows the highest values around the lake edges, where small differences in geolocation between the two methods cause large differences in elevation. The smallest elevation differences are over the flat lake ice area in the center of the DEM. The area in the upper left (northwest) with rounded features in slightly translucent lake ice appears to have more noise compared to other areas. The reasons for that remain unclear. The larger difference of 0.18 m between the DEMs when compared to the 0.09 m difference with the lidar point clouds may reflect the overall accuracy of the methods applied to our data.

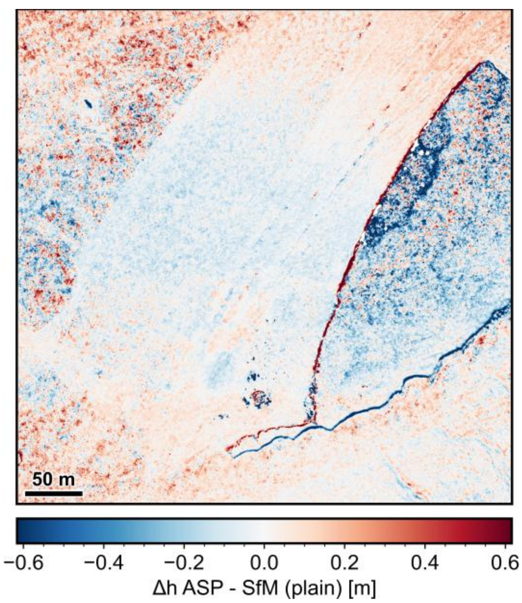

Figure 9: Elevation difference Δh between the plain ASP stereo and SfM DEMs over Lake NW.

https://doi.org/10.5194/egusphere-2026-4143
Preprint. Discussion started: 17 August 2026

4.1.3 Comparison of bathymetry estimates

For the stereo bathymetry processing of Lake NW, we have identified the water pixels in each image with the $NDWI_{ice}$ approach as input for the SAM refinement. The challenging part was to define the water surface elevation for bathymetry processing. Because of the varying elevation biases from differential penetration, we did not use the lidar water surface elevation. Instead, we follow the approach of Dietrich (2026) to determine the water surface elevation consistent with the plain processed DEMs from cross sections over the lake edges in both the stereo and SfM DEMs. Figure 10 shows the bathymetry calculated from stereo processing with ASP's bathymetry module (a) and the bathymetry estimated from SfM processing using pyBathySfM for refraction correction (b). Both elevation models show similar structures with shallow water depths near the shore and a deep basin with water depths up to 7.5 m. Both methods also resolve bottom crevasses visible in the imagery. The lidar point cloud only covers the shallow parts of the lake without lidar returns in a crevasse and a narrow band of lower bathymetry. The elevation differences show no discernible spatial patterns and instead appear to reflect random noise inherent in the data and methods. The elevation difference Δh between the stereo bathymetry and lidar bathymetry has a standard deviation of 0.12 m, with minimum and maximum values of -0.35 m and 0.37 m, respectively (Figure 10a). For the corrected SfM bathymetry, the standard deviation of Δh is 0.13 m with minimum and maximum values of -0.44 m and 0.45 m, respectively (Figure 10b). The 1-σ elevation difference of both the stereo and SfM derived bathymetry is slightly bigger than the 1-σ difference of the plain processed DEMs compared to the lidar ice surface (Δh = 0.09 m). There are several possible reasons for this: First, the slightly steeper terrain at the lake bottom could contribute to larger elevation errors resulting from errors in geolocation of each method. Second, bathymetric processing of the lidar point cloud may introduce additional uncertainties compared to the standard processing, increasing elevation errors in the bathymetry lidar point cloud compared to the ice surface. One reason is that not all lidar waveforms have surface and bottom returns. For the waveforms with only bottom returns we use a mean water surface elevation from the points with surface return slightly increasing elevation uncertainty (Studinger et al., 2022a). Third, applying refraction correction to stereo and SfM DEMs likely increases elevation errors from several sources, such as the uncertainty in water surface elevation used for processing. The SfM refraction correction is an iterative process (Dietrich, 2017) that requires smoothing which could also increase elevation error. Most likely all three sources contribute to the overall increase in elevation errors of the bathymetry grids.

Lastly, we compare the bathymetry DEMs of the stereo and SfM approaches directly (Figure 10c). We have removed outliers around the lake edges that are caused by small geolocation errors over steep elevation gradients because they do not represent the accuracy of the two methods over typical lake bottom relief. The elevation differences Δh appear to be mostly random, however, there seems to be a slight increase in variability towards deeper lake bottom elevations that follows the elevation contours of the DEMs. This change is most pronounced over the deepest part of the lake basin. The histogram of Δh has a standard deviation of 0.32 m, which is again higher than the difference between the plain DEMs over the lake of 0.26 m (Figure 10c) and likely reflects additional elevation uncertainty introduced from the refraction correction.

https://doi.org/10.5194/egusphere-2026-4143
Preprint. Discussion started: 17 August 2026

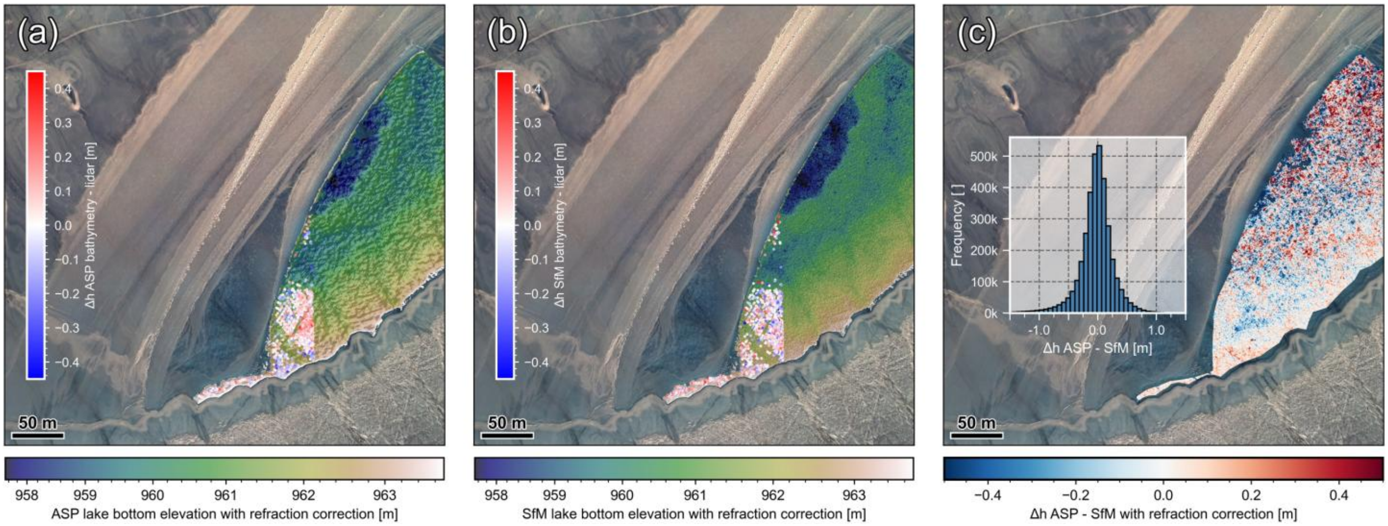

Figure 10: Lake bottom topography for Lake NW with elevation difference Δh between image-based and lidar methods. (a) ASP stereo processing with bathymetry module. (b) SfM processing with pyBathySfM refraction correction. (c) Δh between stereo and SfM processing.

4.2 Lake CW

Lake CW in central west Greenland (Figure 2a) has different challenges for bathymetric processing than Lake NW. Lake CW is surrounded by several small bodies of water with different lake elevations (Figure 11). There is no newly formed thin ice covering this lake, but there are several small ice floes that do not pose a challenge for bathymetric processing since they do not bias lidar elevations and are properly identified as snow and ice surface pixels during $NDWI_{ice}$ classification (Figure 11a). The main challenge for Lake CW is the presence of wind-induced capillary waves on the surface of the lake. The waves themselves are not visible in the images. The refraction of incident sunlight on these waves creates a pattern of highly variable, localized spikes of concentrated illumination on the lake bottom, known as caustics. Caustics can be seen in natural color images as spatially varying brightness patterns on the lake bottom (Figure 11a). These features are not stationary and vary in location and appearance even over the short time between successive image acquisitions. Little is known about the basic characteristics of surface waves on supraglacial lakes, including their amplitude, wavelength, and propagation speed. We attempted to use the lidar point clouds, which have approximate footprints of 0.6 m, to estimate some of these parameters from lake surface returns. However, as expected, the lidar data do not reveal clearly identifiable features from which amplitude, wavelength, or propagation speed of the surface waves—and the resulting caustics on the lake bottom—could be extracted. Because caustics are highly non-stationary, they degrade the performance of image-matching algorithms used in SfM and stereo reconstruction: algorithms either fail to detect sufficient interest points between image pairs or introduce substantial noise into the DEMs from false correlations.

https://doi.org/10.5194/egusphere-2026-4143
Preprint. Discussion started: 17 August 2026

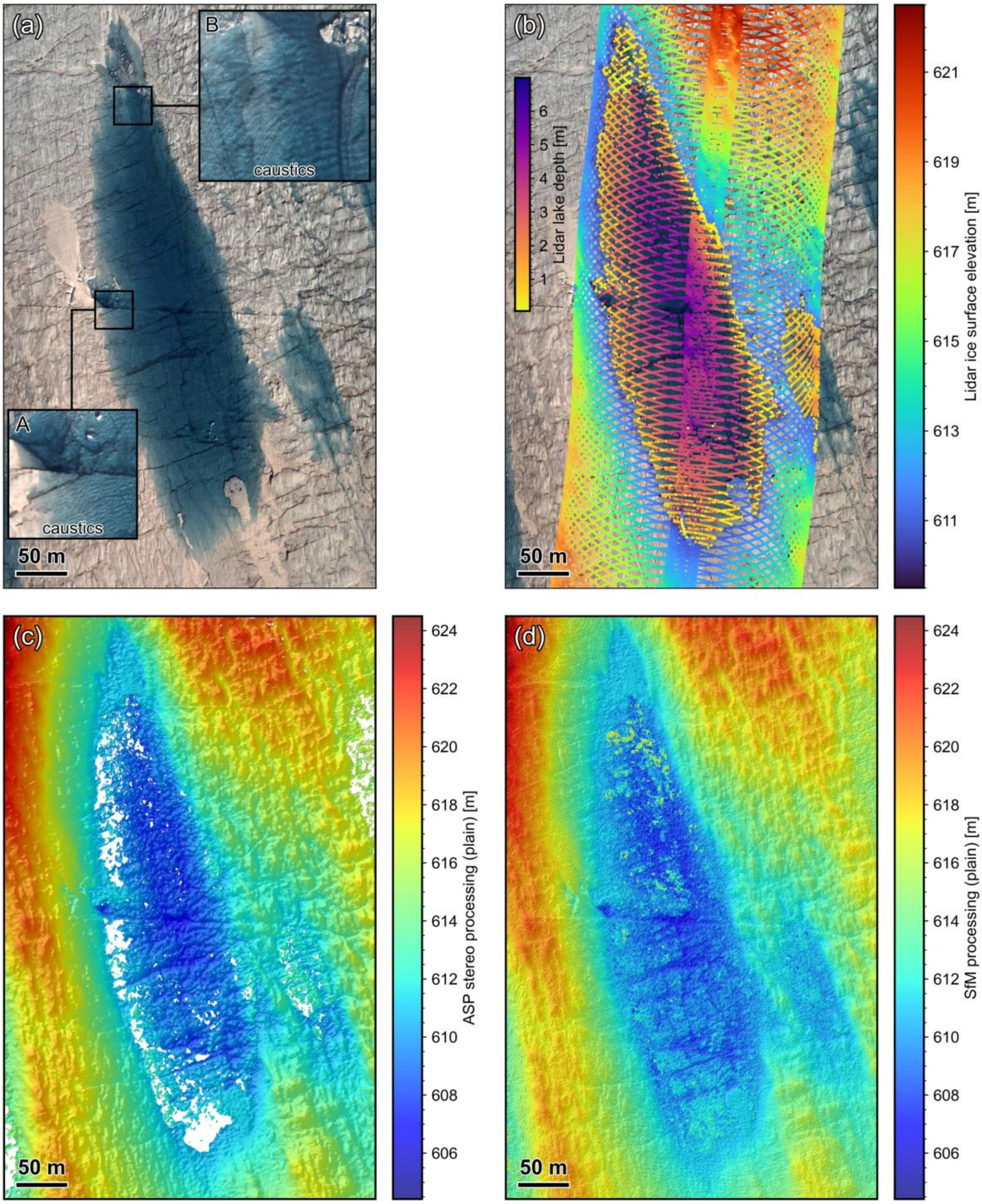

510 **Figure 11:** Lake CW stereo and SfM results without refraction correction (plain). For location of the lake see Figure 2a. (a) Natural color image mosaic. Inset maps show caustics on the lake bottom from single images. (b) Lidar point cloud and lidar-derived bathymetry. (c) DEM from stereo processing. (d) DEM from SfM processing. A version of Figure 11 using CVD-friendly color palettes for panels (b), (c), and (d) is provided in Figure.

https://doi.org/10.5194/egusphere-2026-4143
Preprint. Discussion started: 17 August 2026

We applied the same processing approach to Lake CW as to Lake NW using 11 consecutive images. The only difference is that both bathymetry DEMs were aligned to the lidar ice surface elevation outside the lake, due to substantial elevation errors over the lake that are likely caused by caustics, as discussed below. Lake CW is fully covered by the lidar point cloud from both scanners and shows water depths of over 6 m (Figure 11b). The main features of this lake from imagery and lidar mapping were previously described by Studinger et al. (2022a). We again first use the plain stereo and SfM processed DEMs without refraction correction for a direct comparison. The stereo DEM from plain stereo processing shows the same general structure that can be seen in the visible image mosaic and lidar lake depth including several deep bottom crevasses (Figure 11). However, the DEM shows areas with significant data gaps where the matching algorithm did not detect the same feature in subsequent images due to the non-stationary nature of the caustics. The SfM DEM does not contain data gaps but appears to have significant elevation errors over the main lake. SfM processing resolves the same general structure as seen in visual images, lidar lake depth and stereo DEM, including bottom crevasses. However, over large parts of the lake the SfM DEM shows elevations above the water surface in areas where caustics can be seen in the imagery. Instead of detecting noise from caustics and excluding these areas, SfM appears to derive elevations that contain large errors.

The elevation difference Δh between the plain DEMs shows significantly larger values over the water bodies within the area and good agreement over snow and ice surfaces (Figure 12). Over the main lake elevation differences are significantly higher compared to Lake NW with no caustics. The differences are smallest over the deep crevasses that show no caustics. Over the deep crevasses we do not observe the caustic pattern (inset map A in Figure 11a). It is unclear whether the absence of caustic patterns in bottom crevasses is specific to the circumstances of this lake or a more general phenomenon. The caustics are mostly visible in the shallow parts of the lake. We hypothesize that two factors contribute to that pattern: First the formation and wavelength of wind-induced surface waves could be related to water depth. Second, the deepest parts are often dark crevasses with steep topography that could weaken the optical effect of caustics compared to flat lake bottom (inset map A in Figure 11a).

The lake bottom DEMs with refraction correction both show similar structures as the plain DEMs (Figure 13). For SfM processing with pyBathySfM we have filtered out erroneous pixels above the water surface elevation, since the refraction correction will not return correct lake bottom elevations for these areas. Both DEMs resolve the pattern of bottom crevasses visible in the imagery and lidar point cloud (Figure 11). The elevation difference Δh between the lake bottom DEMs and the lidar lake bottom elevation shows much larger values compared to Lake NW because of the caustics (Figure 13). This is also the case for the lake bottom elevation differences between stereo and SfM (Figure 14).

The refraction correction for all three methods assumes a flat, horizontal water surface without surface waves. Among the three methods, the lidar-derived depths most closely match the water-depth patterns suggested by color variations in the imagery (Figure 11), however, the true lake bottom topography is not known. A possible explanation is that the photons within a laser footprint on the water surface average any topography from waves and resulting refraction within the footprint area (64 cm), which could reduce some of the noise introduced by surface waves depending on their wavelength. The refraction correction for the lidar is applied in the time domain and therefore changes the range (Figure 4). An uneven or tilted water

https://doi.org/10.5194/egusphere-2026-4143
Preprint. Discussion started: 17 August 2026

surface alters the refraction geometry, producing a shift in the apparent location of the laser footprint on the lake bottom. The magnitude of this shift increases with the angle of incidence of the lidar beam on the water surface. This in turn increases errors in water depth. We therefore assume that bathymetry estimates from the narrow scanner (T7) with an off-nadir angle of 2.5° are less impacted by surface waves than the wide scanner (T6), which has an off-nadir angle of 15°. Another source of error comes from the fact that not all lidar lake bottom returns have a water surface return. To use these lidar pulses we calculate the intersection of the lidar beam with a mean water surface elevation, which in the presence of surface waves does not necessarily reflect the actual elevation at the intersection (Studinger et al., 2026a). The standard deviation of the water surface lidar returns for Lake CW is ±0.03 m and slightly larger than ±0.02 m for Lake NW. The larger standard deviation for Lake CW is potentially caused by the presence of surface waves. However, we cannot rule out that improvements made to the lidar instruments also might contribute to the smaller standard deviation over Lake NW.

The refraction correction for stereophotogrammetry and SfM uses the spatial domain (Figure 4). The geometry of the light rays between the camera, water surface and feature on the lake bottom is used. Rays from image pairs taken from different locations in Point A and B intersect different locations on the water surface and will likely have different errors in angle of incidence when surface waves are present (Figure 4). The resulting depth error increases with increasing angles of incidence and is therefore counteracting better vertical accuracy for larger convergence angles.

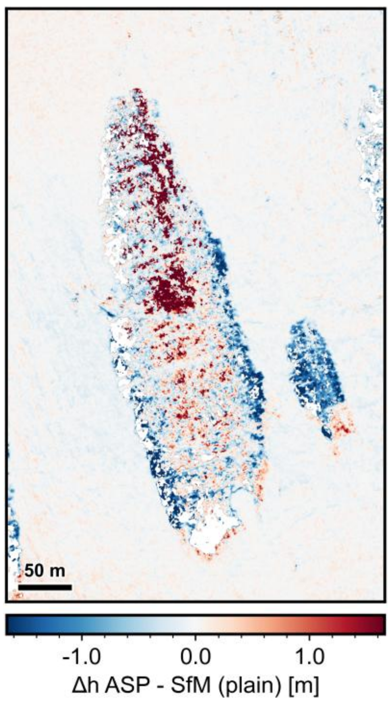

Figure 12: Elevation difference Δh between the plain ASP stereo and SfM DEMs over Lake CW.

https://doi.org/10.5194/egusphere-2026-4143
Preprint. Discussion started: 17 August 2026

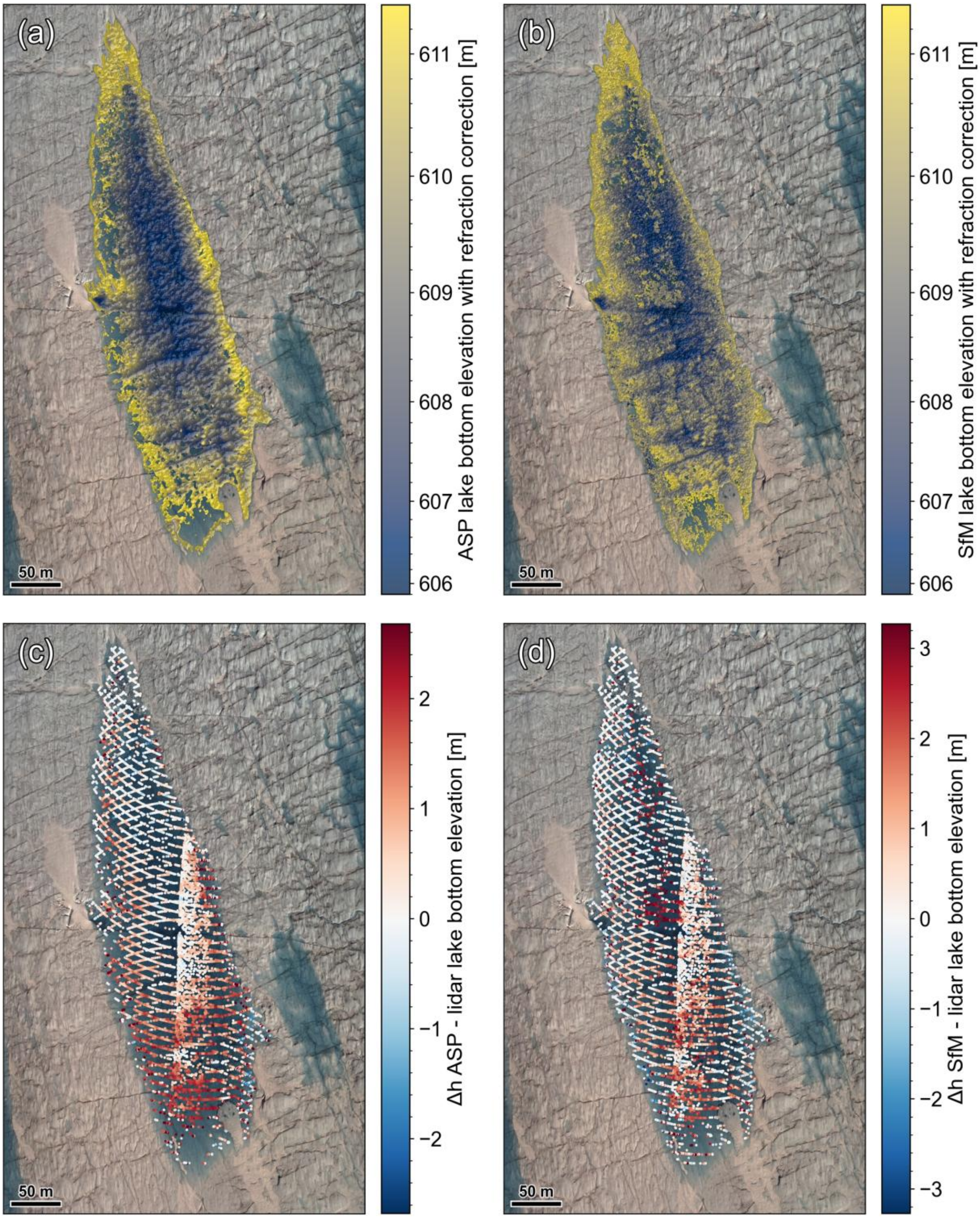

565 **Figure 13:** Lake bottom topography for Lake CW with elevation difference Δh between the image-based methods and lidar point clouds. (a) Stereo processing with bathymetry module and refraction correction. (b) SfM processing with pyBathySfM refraction correction applied. (c) Δh between stereo bathymetry and lidar point cloud. (d) Same for the SfM DEM with pyBathySfM refraction correction.

https://doi.org/10.5194/egusphere-2026-4143
Preprint. Discussion started: 17 August 2026

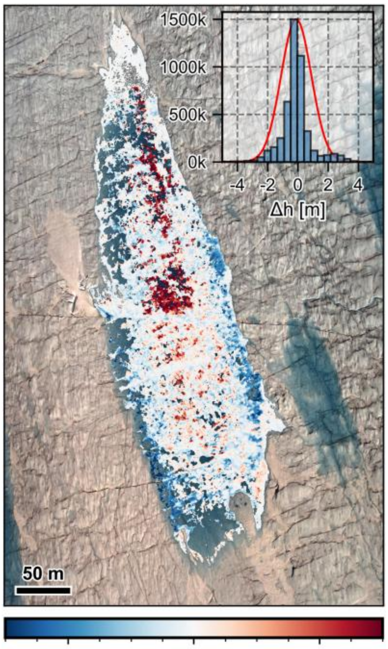

Figure 14: Elevation difference Δh over Lake CW between the lake bottom elevation from ASP stereo processing and SfM with refraction correction applied. Inset shows histogram distribution of Δh with normal distribution (red curve).

5 Discussion and remaining challenges

Our results show that stereophotogrammetry and SfM can be used to derive high-resolution bathymetry of supraglacial lakes on the Greenland Ice Sheet using aerial images, even for data acquisitions that have not been specifically designed for the purpose. We compared two different image-based approaches to bathymetry derived from topobathymetric lidars. Our evaluation shows that image-based methods can produce bathymetry at higher spatial resolution than lidar-derived bathymetry, making them suitable for process-related studies and scientific applications that require high resolution detail. To our knowledge, our work is the first attempt to use airborne imagery for bathymetric mapping of supraglacial lakes on the GrIS and a comparison with coincident lidar-derived topo bathymetry.

Our comparison shows that each method has its unique challenges and limitations that we have discussed in the result sections. For the image-based methods caustics caused by surface waves are the main limitation. There are currently no solutions available that can address surface waves and the resulting caustics, but two avenues of research can be explored. The first one is to potentially turn caustics from noise into a signal using synchronized image acquisitions from two spatially separated platforms from different locations. This could be accomplished with small drone surveys. For piloted aircraft surveys, this will require two or more airplanes, significantly increasing cost and logistics. Simultaneous image acquisitions from different locations can likely address the non-stationary issue of caustics. However, the refraction on a wave-distorted water

https://doi.org/10.5194/egusphere-2026-4143
Preprint. Discussion started: 17 August 2026

surface and the resulting impact on the location of the caustic pattern on the lake bottom, with different ray paths from different camera locations will likely remain a limitation and impacting accuracy. The second possibility is a method called airborne fluid lensing that can remove distortions caused by refraction of light on surface waves (e.g., Bouchelaghem et al., 2026; Chirayath and Earle, 2016) and has been used to create bathymetric DEMs for shallow water from airborne data (Chirayath and Instrella, 2019).

Man et al. (2025) summarized the three main remote sensing bathymetry methods commonly used for supraglacial lake studies: empirical formula method (EFM), radiative transfer method (RTM) and depression topography method (DTM). The EFM uses statistical relationships between water depth and image reflectance. The relationships are derived using independent bathymetry estimates such as ICESat-2. The RTM uses physical models of light propagation in water to determine the distance light has traveled in water, based on the spectral band and assumed optical properties of the water column. The DTM is based on high-quality DEMs of empty lake basins after a lake has drained. It determines a lake shoreline location from remote sensing imagery when the lake basin is filled with water, and the elevation of the water surface can be determined from the drained lake DEM. For a comprehensive discussion of assumptions, limitations, and biases of each method we refer to Man et al. (2025). The three different methods discussed in Man et al. (2025) have limitations in common with the methods discussed here: the presence of surface waves and thin ice cover. There are currently no solutions available that can address these challenges for any of the methods.

We have observed and documented for the first time subsurface volume scattering of green laser light within the lake bottom of a supraglacial lake. We are not aware the depth bias from subsurface volume scattering has been described or evaluated for lake or sea ice melt ponds depths derived from ICESat-2. Since ICESat-2 and the ATM lidars use the same wavelength (532 nm) the interaction of green photons with ice is the same and some bias can be expected in ICESat-2 data. In addition to the bias from the physical interaction between photons and ice are differences from the different retrieval algorithms used to determine the interface (Smith et al., 2025; Studinger et al., 2024). While the estimated bias is relatively small in the ATM data and is approaching the measurement accuracy (Figure 8) we hypothesize that the depth bias from subsurface volume scattering likely plays a larger role in very shallow lakes and sea ice melt ponds.

Advancing our understanding of the interconnected, complex, hydrological system of the GrIS requires improvements in both temporal and spatial detail to enable sophisticated hydrological modeling of the processes and mass fluxes. As can be seen in the image of Lake CW (Figure 11), supraglacial lakes often occur in groups connected by streams. The water bodies have often different water elevations requiring individual treatment for bathymetry estimates in both stereo and SfM processing. It will be challenging to develop an automated processing pipeline that can handle tens of thousands of images acquired during a survey flight and subsequently entire campaigns that are often repeated on an annual basis. In terms of temporal evolution, the time between satellite passes or airborne repeat flights is likely not sufficient to fully capture the seasonal changes in water level and size of the lakes, limiting our understanding of these features and how they respond to environmental drivers.

https://doi.org/10.5194/egusphere-2026-4143
Preprint. Discussion started: 17 August 2026

While space-based methods have the advantage of good spatial and temporal coverage, their limited spatial resolution is not suitable for every research application. Aerial imagery taken from conventional aircraft or small uncrewed aerial platforms can complement the spaceborne bathymetry estimates, particularly when combined with data from topobathymetric lidars collected from the same platform. Broadening science applications with high-resolution data will advance our understanding of the hydrological system of ice sheets and in turn provide more accurate mass balance estimates that are required for sea level projections.

6 Conclusions

Our results show that supraglacial lake bathymetry can be mapped at high spatial resolution using stereophotogrammetry and SfM reconstruction of topobathymetric DEMs. The stereographic method we use accurately accounts for refraction in water (Palaseanu-Lovejoy et al., 2023). The SfM approach uses an iterative refraction correction for SfM to accurately determine the lake bottom topography (Dietrich, 2017). We have compared the results from the two image-based methods with each other and with coincident bathymetry estimates from topobathymetric lidars with accurate three-dimensional refraction correction applied. Because of the limited availability of opportunistic airborne data, we do not have a robust estimate of how surface waves, caustics, steep crevasses and other factors impact the accuracy of the three different bathymetry estimates. However, all three methods show generally good agreement when no surface waves are present and in areas with no abrupt elevation changes.

Each method has its own limitations and biases. By analyzing changes in the shape of lidar waveforms between survey targets with no differential penetration and supraglacial lakes we have shown for the first time that green photons can penetrate below the lake bottom surface resulting in a range and therefore elevation bias. The effect we observed, however, is small and comparable to the vertical uncertainty of the lidar instruments used.

The high spatial resolution that can be achieved with image-based methods can currently not be replicated with existing state-of-the-art topobathymetric portions of topobathymetric lidars due to the beam divergence of existing lidars and the resulting footprint size. Furthermore, lidar pulse repetition rates of currently available airborne lidars are not sufficient for achieving the same high point density as in optical images. However, continuing improvements in lidar pulse repetition rate, and beam divergence, and multi-segment detection will likely narrow that gap going forward.

We used aerial imagery and lidar data for this study that were not specifically designed or intended to be used for bathymetric mapping. In terms of survey design, long flight lines with no lateral overlap between images are known to be problematic for stereo and SfM processing, which is the typical regional aerial survey design because of cost considerations. However, we have shown that this limitation can be largely overcome with accurate trajectory and attitude data and camera calibration. We can expect that dedicated survey and instrument design will improve the accuracy of these methods. There are currently no solutions for limitations like thin ice cover, surface waves, and caustics, which also impact many of the spaceborne methods discussed in this paper. The accuracy and spatial resolution demonstrated here shows that bathymetric mapping from

https://doi.org/10.5194/egusphere-2026-4143
Preprint. Discussion started: 17 August 2026

aerial imagery can make an important contribution to studying supraglacial lakes and advance our knowledge and understanding of the hydrological system of the GrIS.

https://doi.org/10.5194/egusphere-2026-4143
Preprint. Discussion started: 17 August 2026

Appendix A

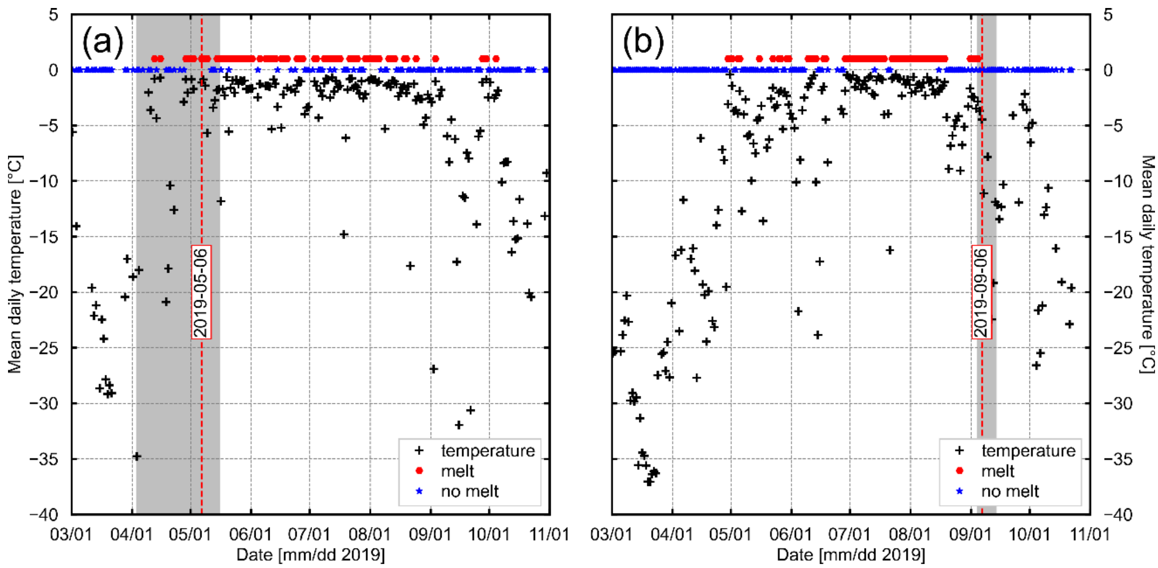

Figure A1: Surface temperature (black crosses) from the Moderate Resolution Imaging Spectroradiometer (MODIS) with surface melt indicators (red circles and blue stars) for the two campaigns (gray boxes) at the locations of the two lakes (Hall and DiGirolamo, 2019; Hall et al., 2018) shown in Figure 2. Dashed vertical lines mark the days of airborne data acquisition over the lakes. (a) Lake NW and (b) Lake CW.

https://doi.org/10.5194/egusphere-2026-4143
Preprint. Discussion started: 17 August 2026

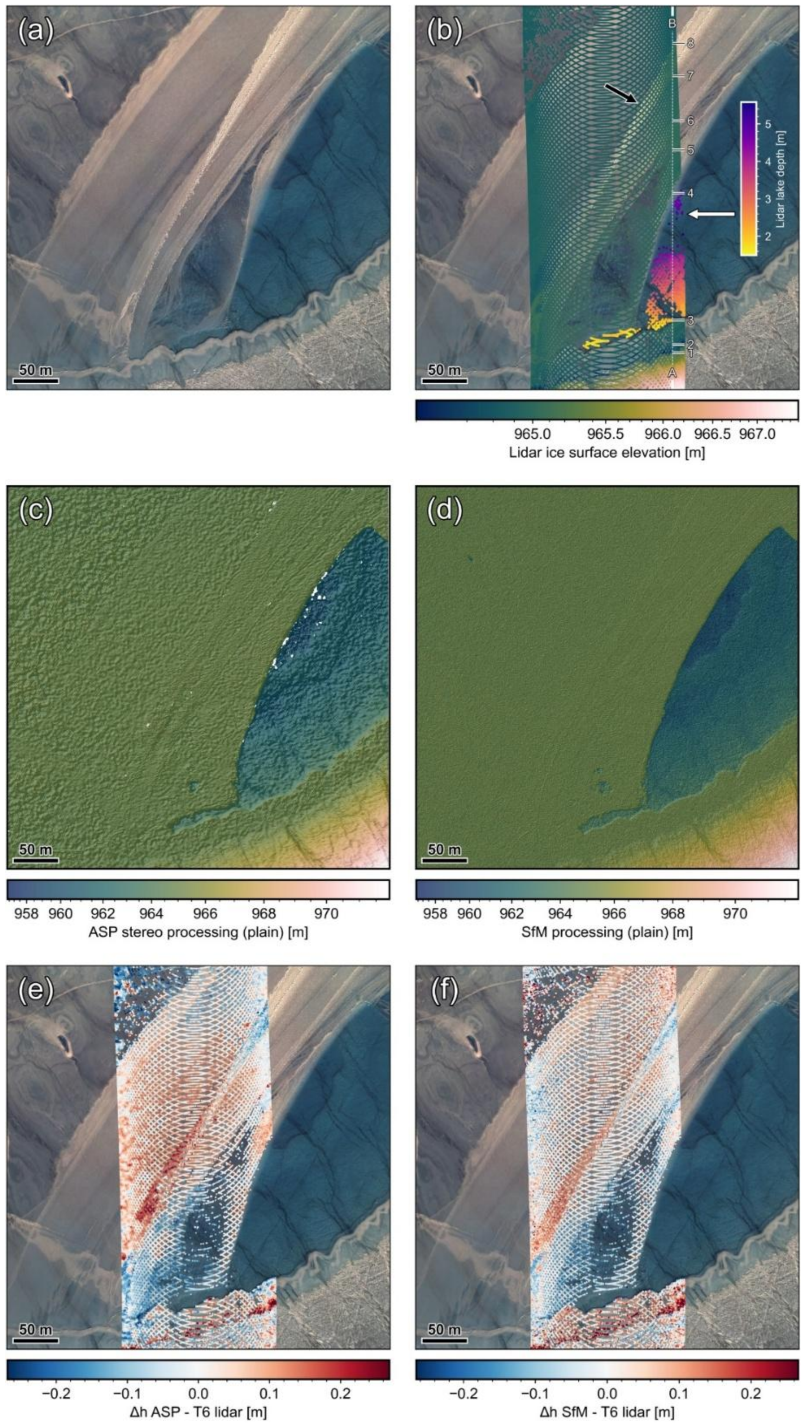

Figure A2: Alternative version of Figure 6 using CVD-friendly color palettes from Crameri **(2023)**. Lake NW stereo and SfM results without refraction correction (plain). For location of the lake see Figure 2b. (a) Natural color image mosaic. (b) Lidar point cloud and lidar-derived bathymetry with location of profile shown in Figure 7. (c) DEM from stereo processing. (d) DEM from SfM processing. (e) Elevation difference Δh between stere DEM and lidar point cloud and same for SfM (f).

https://doi.org/10.5194/egusphere-2026-4143
Preprint. Discussion started: 17 August 2026

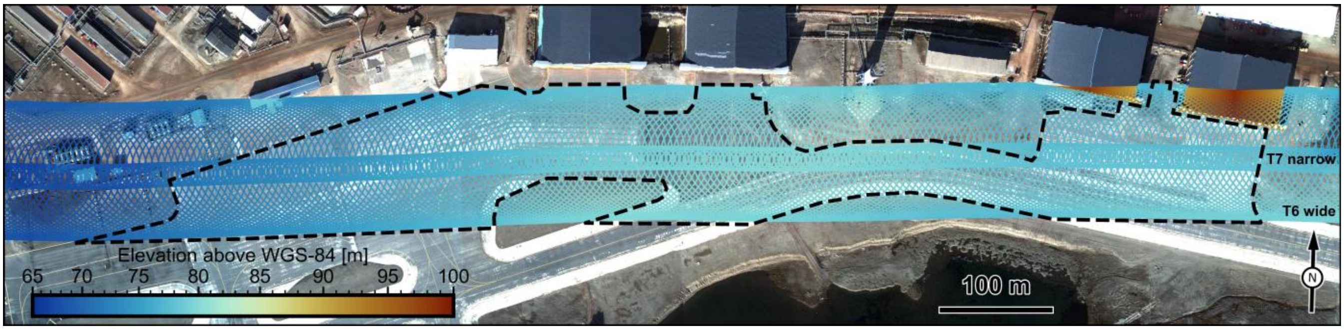

Figure A3: Airport ramp at Pituffik Space Base in northwest Greenland (formerly Thule Air Base). The flat concrete area on the ramp that is used for range calibration and bias monitoring of the two lidars is outlined by a black dashed line with elevations from the wide scan T6 and narrow scan T7 lidar point clouds. Background image is a natural color image mosaic of 16 CAMBOT L1-B images from the overpass on 9 September 2019 spanning 1240 × 300 m. The image mosaic is available as part of this paper (Studinger et al., 2026b).

https://doi.org/10.5194/egusphere-2026-4143
Preprint. Discussion started: 17 August 2026

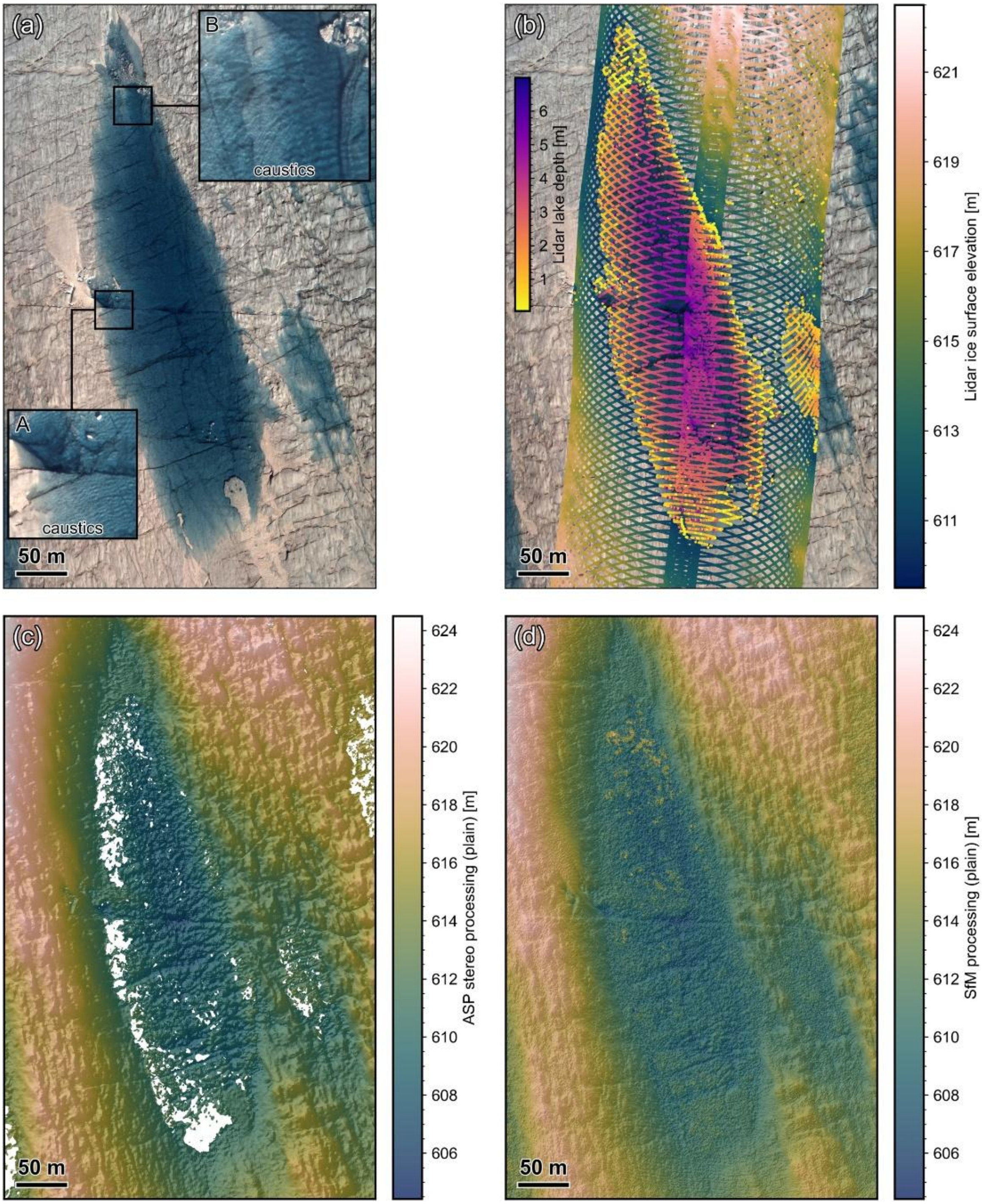

675 **Figure A4:** Alternative version of Figure 11 using CVD-friendly color palettes from Crameri (2023). Lake CW stereo and SfM results without refraction correction (plain). For location of the lake see Figure 2a. (a) Natural color image mosaic. Inset maps show caustics on the lake bottom from single images. (b) Lidar point cloud and lidar-derived bathymetry. (c) DEM from stereo processing. (d) DEM from SfM processing.

https://doi.org/10.5194/egusphere-2026-4143
Preprint. Discussion started: 17 August 2026

Code and data availability:

Code: The Python™ code and tutorials developed for this work are available at https://doi.org/10.5281/zenodo.18924664 (Studinger et al., 2026a). The MATLAB® code for lidar processing was previously described and published (Studinger et al., 2022a) and is available at: https://doi.org/10.5281/zenodo.6341230 (Studinger, 2022).

Data: NASA's Operation IceBridge airborne data products are available at the NSIDC (https://nsidc.org) and through NASA Earthdata (https://www.earthdata.nasa.gov/). The lidar range calibration data previously published (Studinger et al., 2022b) is available at together with MATLAB® code: https://doi.org/10.5281/zenodo.7225937. Camera files and trajectories used in this paper are published as part of this paper at: https://doi.org/10.5281/zenodo.21111997 (Studinger et al., 2026b).

This study uses Sentinel-2 data from the European Space Agency's Copernicus program, which is available at https://dataspace.copernicus.eu/explore-data/data-collections/sentinel-data/sentinel-2 (European Space Agency (ESA), 2025). The ice surface temperature and ice surface melt indicator from MODIS (Hall and DiGirolamo, 2019; Hall et al., 2018) are available at NSIDC at https://doi.org/10.5067/7THUWT9NMPDK (Hall and DiGirolamo, 2019).

Author contributions

MS led the analysis of the lidar and optical imagery, integration of results, and preparation of the manuscript. CWW led the processing and analysis of SfM data and results and OA helped with stereo processing and analysis. All authors helped develop the study, interpret the results, and commented on the manuscript.

Competing interests

The contact author has declared that none of the authors has any competing interests.

Acknowledgements

The work presented in this paper was made possible by the combined efforts of all ATM team members developing instruments and data products and collecting data over the course of many years. Matt Linkswiler, Kyle Krabill, and John Sonntag are thanked particularly for discussions about GPS trajectories. Jeremy Harbeck is thanked for discussions about ground control points. David Shean, Christopher Parrish, and Shashank Bhushan are thanked for discussions about stereo and SfM processing. We thank the Operation Ice Bridge flight crews for many years of data collection.

Financial support

This work was funded by NASA's Internal Scientist Funding Model (MS and CWW), the Airborne Science Program, and the Cryospheric Sciences Program.

References

Agarwal, S., Mierle, K., and Team, T. C. S.: Ceres Solver, 2023.

Alexandrov, O., McMichael, S., Broxton, M., Lundy, M., Beyer, R., Husmann, K., Edwards, L., Nefian, A., Smith, Benjamin, Shean, D., Smith, T., mstyer, Annex, A., Purinton, B., Bertone, S., drpeachboy, Dehecq, A., Nodjoumi, G., Aravkin, A., Bhushan, S., Moratto, Z., Meyer, J., PicoJr, and Laura, J.: NeoGeographyToolkit/StereoPipeline: 2026-03-30-daily-build, , https://doi.org/10.5281/ZENODO.598174, 2026.

Allied Vision: Prosilica GT 4905 Data Sheet, 2022.

Arndt, P. S. and Fricker, H. A.: A framework for automated supraglacial lake detection and depth retrieval in ICESat-2 photon data across the Greenland and Antarctic ice sheets, The Cryosphere, 18, 5173–5206, https://doi.org/10.5194/tc-18-5173-2024, 2024.

Beyer, R. A., Alexandrov, O., and McMichael, S.: The Ames Stereo Pipeline: NASA's Open Source Software for Deriving and Processing Terrain Data, Earth Space Sci., 5, 537–548, https://doi.org/10.1029/2018EA000409, 2018.

Bjørk, A. A., Kruse, L. M., and Michaelsen, P. B.: Brief communication: Getting Greenland's glaciers right – a new data set of all official Greenlandic glacier names, The Cryosphere, 9, 2215–2218, https://doi.org/10.5194/tc-9-2215-2015, 2015.

Bouchelaghem, S., Chirayath, V., Tibermacine, I. E., Dempsey, A. C., and Purkis, S. J.: Cm-scale marine habitat mapping of entire Tumon Bay, Guam Coral Reef using NASA airborne fluid lensing and NeMO-Net pre (2022) and post (2024) Typhoon Mawar, Front. Mar. Sci., 13, 1785978, https://doi.org/10.3389/fmars.2026.1785978, 2026.

Bradski, G.: The Opencv Library, 2000.

Brenner, A. C., Zwally, H. J., Bentley, C. R., Csatho, B. M., Harding, D. J., Hofton, M. A., Minster, J.-B., Roberts, L., Saba, J. L., Thomas, R. H., and Yi, D.: The Algorithm Theoretical Basis Document for the Derivation of Range and Range Distributions from Laser Pulse Waveform Analysis for Surface Elevations, Roughness, Slope, and Vegetation Heights, NASA GSFC, Goddard Space Flight Center, 2012.

Chirayath, V. and Earle, S. A.: Drones that see through waves – preliminary results from airborne fluid lensing for centimetre-scale aquatic conservation, Aquat. Conserv. Mar. Freshw. Ecosyst., 26, 237–250, https://doi.org/10.1002/aqc.2654, 2016.

Chirayath, V. and Instrella, R.: Fluid lensing and machine learning for centimeter-resolution airborne assessment of coral reefs in American Samoa, Remote Sens. Environ., 235, 111475, https://doi.org/10.1016/j.rse.2019.111475, 2019.

Chu, V. W.: Greenland ice sheet hydrology: A review, Prog. Phys. Geogr. Earth Environ., 38, 19–54, https://doi.org/10.1177/0309133313507075, 2014.

Crameri, F.: Scientific colour maps, , https://doi.org/10.5281/ZENODO.8409685, 2023.

Datta, R. T. and Wouters, B.: Supraglacial lake bathymetry automatically derived from ICESat-2 constraining lake depth estimates from multi-source satellite imagery, The Cryosphere, 15, 5115–5132, https://doi.org/10.5194/tc-15-5115-2021, 2021.

Dietrich, J.: geojames/pyBathySfM: Version 7.0, , https://doi.org/10.5281/ZENODO.3377601, 2026.

Dietrich, J. T.: Bathymetric Structure-from-Motion: extracting shallow stream bathymetry from multi-view stereo photogrammetry, Earth Surf. Process. Landf., 42, 355–364, https://doi.org/10.1002/esp.4060, 2017.

Dietrich, J. T. and Parrish, C. E.: Development and Analysis of a Global Refractive Index of Water Data Layer for Spaceborne and Airborne Bathymetric Lidar, Earth Space Sci., 12, e2024EA004106, https://doi.org/10.1029/2024EA004106, 2025.

Enderlin, E. M., Howat, I. M., Jeong, S., Noh, M., Van Angelen, J. H., and Van Den Broeke, M. R.: An improved mass budget for the Greenland ice sheet, Geophys. Res. Lett., 41, 866–872, https://doi.org/10.1002/2013GL059010, 2014.

European Space Agency (ESA): Sentinel-2 Level-2A data, 2025.

Facciolo, G., Franchis, C. D., and Meinhardt, E.: MGM: A Significantly More Global Matching for Stereovision, in: Procedings of the British Machine Vision Conference 2015, British Machine Vision Conference 2015, 90.1-90.12, https://doi.org/10.5244/C.29.90, 2015.

Fair, Z., Flanner, M., Brunt, K. M., Fricker, H. A., and Gardner, A.: Using ICESat-2 and Operation IceBridge altimetry for supraglacial lake depth retrievals, The Cryosphere, 14, 4253–4263, https://doi.org/10.5194/tc-14-4253-2020, 2020.

Fair, Z., Flanner, M., Neumann, T., Vuyovich, C., Smith, B., and Schneider, A.: Quantifying Volumetric Scattering Bias in ICESat-2 and Operation IceBridge Altimetry Over Greenland Firn and Aged Snow, Earth Space Sci., 11, e2022EA002479, https://doi.org/10.1029/2022EA002479, 2024.

Fuchs, N., Von Albedyll, L., Birnbaum, G., Linhardt, F., Oppelt, N., and Haas, C.: Sea ice melt pond bathymetry reconstructed from aerial photographs using photogrammetry: a new method applied to MOSAiC data, The Cryosphere, 18, 2991–3015, https://doi.org/10.5194/tc-18-2991-2024, 2024.

Hall, D. and DiGirolamo, N.: Multilayer Greenland Ice Surface Temperature, Surface Albedo, and Water Vapor from MODIS, Version 1, https://doi.org/10.5067/7THUWT9NMPDK, 2019.

Hall, D. K., Cullather, R. I., DiGirolamo, N. E., Comiso, J. C., Medley, B. C., and Nowicki, S. M.: A Multilayer Surface Temperature, Surface Albedo, and Water Vapor Product of Greenland from MODIS, Remote Sens., 10, 555, https://doi.org/10.3390/rs10040555, 2018.

Howat, I. M., Negrete, A., and Smith, B. E.: The Greenland Ice Mapping Project (GIMP) land classification and surface elevation data sets, The Cryosphere, 8, 1509–1518, https://doi.org/10.5194/tc-8-1509-2014, 2014.

Kirillov, A., Mintun, E., Ravi, N., Mao, H., Rolland, C., Gustafson, L., Xiao, T., Whitehead, S., Berg, A. C., Lo, W.-Y., Dollár, P., and Girshick, R.: Segment Anything, http://arxiv.org/abs/2304.02643, 5 April 2023.

Liao, P.-S., Chen, T.-S., and Chung, P.-C.: A Fast Algorithm for Multilevel Thresholding, J. Inf. Sci. Eng., 17, https://doi.org/10.6688/JISE.2001.17.5.1, 2001.

MacGregor, J. A., Boisvert, L. N., Medley, B., Petty, A. A., Harbeck, J. P., Bell, R. E., Blair, J. B., Blanchard-Wrigglesworth, E., Buckley, E. M., Christoffersen, M. S., Cochran, J. R., Csathó, B. M., De Marco, E. L., Dominguez, R. T., Fahnestock, M. A., Farrell, S. L., Gogineni, S. P., Greenbaum, J. S., Hansen, C. M., Hofton, M. A., Holt, J. W., Jezek, K. C., Koenig, L. S., Kurtz, N. T., Kwok, R., Larsen, C. F., Leuschen, C. J., Locke, C. D., Manizade, S. S., Martin, S., Neumann, T. A., Nowicki, S. M. J., Paden, J. D., Richter-Menge, J. A., Rignot, E. J., Rodríguez-Morales, F., Siegfried, M. R., Smith, B. E., Sonntag, J. G., Studinger, M., Tinto, K. J., Truffer, M., Wagner, T. P., Woods, J. E., Young, D. A., and Yungel, J. K.: The Scientific Legacy of NASA's Operation IceBridge, Rev. Geophys., 59, e2020RG000712, https://doi.org/10.1029/2020RG000712, 2021.

Man, M., Yang, K., Chen, D., Zhu, Y., and Wang, Y.: Estimating supraglacial lake depth in Greenland: A comparison study of empirical formula, radiative transfer and depression topography methods, J. Glaciol., 71, e41, https://doi.org/10.1017/jog.2025.23, 2025.

Martin, C. F., Krabill, W. B., Manizade, S. S., Russell, R. L., Sonntag, J. G., Swift, R. N., and Yungel, J. K.: Airborne Topographic Mapper Calibration Procedures and Accuracy Assessment, 2012.

Murray, A., Kemenade, H. van, wiredfool, Clark, J. A., Karpinsky, A., Baranovič, O., Yay295, Gohlke, C., Dufresne, J., Brett, M., DWesl, Schmidt, D., Kopachev, K., Houghton, A., REDxEYE, Russell Keith-Magee, Sandro Mani, Steve Landey, Aarni Koskela, Josh Ware, vashek, Piolie, Jason Douglas, Stanislau T, David Caro, Uriel Martinez, and Riley Lahd: python-pillow/Pillow: 12.1.1, , https://doi.org/10.5281/ZENODO.18604291, 2026.

Nienow, P. W., Sole, A. J., Slater, D. A., and Cowton, T. R.: Recent Advances in Our Understanding of the Role of Meltwater in the Greenland Ice Sheet System, Curr. Clim. Change Rep., 3, 330–344, https://doi.org/10.1007/s40641-017-0083-9, 2017.

Otosaka, I. N., Shepherd, A., Ivins, E. R., Schlegel, N.-J., Amory, C., Van Den Broeke, M. R., Horwath, M., Joughin, I., King, M. D., Krinner, G., Nowicki, S., Payne, A. J., Rignot, E., Scambos, T., Simon, K. M., Smith, B. E., Sørensen, L. S., Velicogna, I., Whitehouse, P. L., A, G., Agosta, C., Ahlstrøm, A. P., Blazquez, A., Colgan, W., Engdahl, M. E., Fettweis, X., Forsberg, R., Gallée, H., Gardner, A., Gilbert, L., Gourmelen, N., Groh, A., Gunter, B. C., Harig, C., Helm, V., Khan, S. A., Kittel, C., Konrad, H., Langen, P. L., Lecavalier, B. S., Liang, C.-C., Loomis, B. D., McMillan, M., Melini, D., Mernild, S. H., Mottram, R., Mouginot, J., Nilsson, J., Noël, B., Pattle, M. E., Peltier, W. R., Pie, N., Roca, M., Sasgen, I., Save, H. V., Seo, K.-W., Scheuchl, B., Schrama, E. J. O., Schröder, L., Simonsen, S. B., Slater, T., Spada, G., Sutterley, T. C., Vishwakarma, B. D., Van Wessem, J. M., Wiese, D., Van Der Wal, W., and Wouters, B.: Mass balance of the Greenland and Antarctic ice sheets from 1992 to 2020, Earth Syst. Sci. Data, 15, 1597–1616, https://doi.org/10.5194/essd-15-1597-2023, 2023.

Otsu, N.: A Threshold Selection Method from Gray-Level Histograms, IEEE Trans. Syst. Man Cybern., 9, 62–66, https://doi.org/10.1109/TSMC.1979.4310076, 1979.

Palaseanu-Lovejoy, M., Alexandrov, O., Danielson, J., and Storlazzi, C.: SaTSeaD: Satellite Triangulated Sea Depth Open-Source Bathymetry Module for NASA Ames Stereo Pipeline, Remote Sens., 15, 3950, https://doi.org/10.3390/rs15163950, 2023.

Pitcher, L. H. and Smith, L. C.: Supraglacial Streams and Rivers, Annu. Rev. Earth Planet. Sci., 47, 421–452, https://doi.org/10.1146/annurev-earth-053018-060212, 2019.

Purkis, S. and Klemas, V.: Remote Sensing and Global Environmental Change, 1st ed., Wiley, https://doi.org/10.1002/9781118687659, 2011.

Saha, S., Moorthi, S., Pan, H.-L., Wu, X., Wang, J., Nadiga, S., Tripp, P., Kistler, R., Woollen, J., Behringer, D., Liu, H., Stokes, D., Grumbine, R., Gayno, G., Wang, J., Hou, Y.-T., Chuang, H., Juang, H.-M. H., Sela, J., Iredell, M., Treadon, R., Kleist, D., Van Delst, P., Keyser, D., Derber, J., Ek, M., Meng, J., Wei, H., Yang, R., Lord, S., Van Den Dool, H., Kumar, A., Wang, W., Long, C., Chelliah, M., Xue, Y., Huang, B., Schemm, J.-K., Ebisuzaki, W., Lin, R., Xie, P., Chen, M., Zhou, S., Higgins, W., Zou, C.-Z., Liu, Q., Chen, Y., Han, Y., Cucurull, L., Reynolds, R. W., Rutledge, G., and Goldberg, M.: The NCEP Climate Forecast System Reanalysis, Bull. Am. Meteorol. Soc., 91, 1015–1058, https://doi.org/10.1175/2010BAMS3001.1, 2010.

Slocum, R. K., Wright, W., Parrish, C., Costa, B., Sharr, M., and Battista, T.A.: Guidelines for Bathymetric Mapping and Orthoimage Generation using sUAS and SfM, An Approach for Conducting Nearshore Coastal Mapping, https://doi.org/10.25923/07MX-1F93, 2019.

Smith, B. E., Gardner, A., Schneider, A., and Flanner, M.: Modeling biases in laser-altimetry measurements caused by scattering of green light in snow, Remote Sens. Environ., 215, 398–410, https://doi.org/10.1016/j.rse.2018.06.012, 2018.

Smith, B. E., Studinger, M., Sutterley, T., Fair, Z., and Neumann, T.: Understanding biases in ICESat-2 data due to subsurface scattering using Airborne Topographic Mapper waveform data, The Cryosphere, 19, 975–995, https://doi.org/10.5194/tc-19-975-2025, 2025.

Studinger, M.: IceBridge ATM L1B Elevation and Return Strength with Waveforms, Version 1, https://doi.org/10.5067/EZQ5U3R3XWBS, 2018a.

Studinger, M.: IceBridge Narrow Swath ATM L1B Elevation and Return Strength with Waveforms, Version 1, https://doi.org/10.5067/V25X7LHDPMZY, 2018b.

Studinger, M.: Airborne Topographic Mapper (ATM) Bathymetry Toolkit, , https://doi.org/10.5281/ZENODO.6341229, 2022.

Studinger, M. and Harbeck, J.: IceBridge CAMBOT L1B Geolocated Images, Version 2, https://doi.org/10.5067/B0HL940D452L, 2019.

Studinger, M. and Harbeck, J.: IceBridge CAMBOT L0 Raw Imagery, Version 1, https://doi.org/10.5067/IOJH8A5F48J5, 2020.

Studinger, M., Manizade, S. S., Linkswiler, M. A., and Yungel, J. K.: High-resolution imaging of supraglacial hydrological features on the Greenland Ice Sheet with NASA's Airborne Topographic Mapper (ATM) instrument suite, The Cryosphere, 16, 3649–3668, https://doi.org/10.5194/tc-16-3649-2022, 2022a.

https://doi.org/10.5194/egusphere-2026-4143
Preprint. Discussion started: 17 August 2026

Studinger, M., Linkswiler, M. A., Manizade, S. S., and Yungel, J. K.: NASA's Airborne Topographic Mapper (ATM) ground calibration data for waveform data products (1.0), https://doi.org/10.5281/ZENODO.7225937, 2022b.

Studinger, M., Smith, B. E., Kurtz, N., Petty, A., Sutterley, T., and Tilling, R.: Estimating differential penetration of green (532 nm) laser light over sea ice with NASA's Airborne Topographic Mapper: observations and models, The Cryosphere, 18, 2625–2652, https://doi.org/10.5194/tc-18-2625-2024, 2024.

Studinger, M., Wright, C. W., and Alexandrov, O.: Bathymetry of supraglacial lakes and streams on the Greenland Ice Sheet from high-resolution aerial photography, , https://doi.org/10.5281/ZENODO.18924663, 2026a.

Studinger, M., Harbeck, J., Krabill, K., Linkswiler, M., Sonntag, J., and Wright, C. W.: NASA's Airborne Topographic Mapper (ATM) trajectory and camera data for the Arctic Spring and Fall campaigns 2019 (1.0), https://doi.org/10.5281/ZENODO.21111997, 2026b.

The IMBIE Team: Mass balance of the Greenland Ice Sheet from 1992 to 2018, Nature, 579, 233–239, https://doi.org/10.1038/s41586-019-1855-2, 2020.

Tsai, R.: A versatile camera calibration technique for high-accuracy 3D machine vision metrology using off-the-shelf TV cameras and lenses, IEEE J. Robot. Autom., 3, 323–344, https://doi.org/10.1109/JRA.1987.1087109, 1987.

Van Den Broeke, M. R., Enderlin, E. M., Howat, I. M., Kuipers Munneke, P., Noël, B. P. Y., Van De Berg, W. J., Van Meijgaard, E., and Wouters, B.: On the recent contribution of the Greenland ice sheet to sea level change, The Cryosphere, 10, 1933–1946, https://doi.org/10.5194/tc-10-1933-2016, 2016.

Wehrlé, A., Lüthi, M. P., Kneib-Walter, A., Nap, A., Rousseau, H., Jouvet, G., and Walter, F.: Velocity and calving response of a major Greenland ice stream to a lake drainage event, Nat. Geosci., 19, 84–89, https://doi.org/10.1038/s41561-025-01858-2, 2026.

Woodget, A. S., Carbonneau, P. E., Visser, F., and Maddock, I. P.: Quantifying submerged fluvial topography using hyperspatial resolution UAS imagery and structure from motion photogrammetry, Earth Surf. Process. Landf., 40, 47–64, https://doi.org/10.1002/esp.3613, 2015.

Yang, K. and Smith, L. C.: Supraglacial Streams on the Greenland Ice Sheet Delineated From Combined Spectral–Shape Information in High-Resolution Satellite Imagery, IEEE Geosci. Remote Sens. Lett., 10, 801–805, https://doi.org/10.1109/LGRS.2012.2224316, 2013.